



Review

Recent progress in Li and Mn rich layered oxide cathodes for Li-ion batteries

Yiwei Li^{a,1}, Zhibo Li^{a,1}, Cong Chen^a, Kai Yang^a, Bo Cao^a, Shenyang Xu^a, Ni Yang^a, Wenguang Zhao^a, Haibiao Chen^a, Mingjian Zhang^{a,b,*}, Feng Pan^{a,*}

^aSchool of Advanced Materials, Peking University, Shenzhen Graduate School, Shenzhen 518055, Guangdong, China

^bCenter for Advanced Radiation Source (ChemMatCARS), the University of Chicago, Argonne, IL 60439, United States

ARTICLE INFO

Article history:

Received 14 October 2020

Revised 23 January 2021

Accepted 25 January 2021

Available online 10 February 2021

Keywords:

Li-ion batteries

Li and Mn rich layered oxide cathodes

Electrochemical concerns

Progress and perspective

ABSTRACT

Li and Mn rich (LMR) layered oxides, written as $x\text{Li}_2\text{MnO}_3 \cdot (1-x)\text{LiMO}_2$ ($M = \text{Mn, Ni, Co, Fe, etc.}$), have been widely reported in recent years due to their high capacity and high energy density. The stable structure and superior performance of LMR oxides make them one of the most promising candidates for the next-generation cathode materials. However, the commercialization of these materials is hindered by several drawbacks, such as low initial Coulombic efficiency, the degradation of voltage and capacity during cycling, and poor rate performance. This review summarizes research progress in solving these concerns of LMR cathodes over the past decade by following three classes of strategies: morphology design, bulk design, and surface modification. We elaborate on the processing procedures, electrochemical performance, mechanisms, and limitations of each approach, and finally put forward the concerns left and the possible solutions for the commercialization of LMR cathodes.

© 2021 Science Press and Dalian Institute of Chemical Physics, Chinese Academy of Sciences. Published by ELSEVIER B.V. and Science Press. All rights reserved.



Yiwei Li received his B.S. degree in College of Materials Science and Engineering from Huazhong University of Science and Technology in 2017. He is currently a Ph.D. candidate at School of Advanced Materials, Peking University. His main research work is Li-Rich cathode materials with high voltage and high energy density for Li ion batteries.



Zhibo Li received his B.S. degree from South China Normal University in 2018. He is currently a M.S. student under the supervision of Prof. Feng Pan at School of Advanced Material, Peking University. His research interests mainly focus on layered cathode material for lithium ion batteries.

* Corresponding authors.

E-mail addresses: zhangmj@pkusz.edu.cn (M. Zhang), panfeng@pkusz.edu.cn (F. Pan).

¹ These authors contributed equally to this work.



Cong Chen received his B.S. degree from South China University of Technology in 2018. He is currently a M.S. student under the supervision of Prof. Feng Pan at school of Advanced Material, Peking University. His research interests mainly focus on layered cathode material for lithium ion and sodium ion batteries.



Wenguang Zhao is an engineer at School of Advanced Materials, Peking University Shenzhen Graduate School, China. He has over 10 years' experience in material characterization using wide range of analytical tools including XRD, XPS, SEM and TEM. His research interests mainly focus on the ex/in-situ TEM and ex/in-situ XRD characterization of battery materials.



Kai Yang received his B.S. degree in the School of Aerospace from Tsinghua University in 2016, China. He is pursuing his M.S. degree at School of Advanced Materials, Peking University Shenzhen Graduate School, China. His main research interests include advanced silicon carbon materials for lithium ion batteries (LIBs) and advanced technology for interface research in LIBs, such as in-situ AFM and EQCM.



Haibiao Chen is currently a senior researcher at School of Advanced Materials, Peking University Shenzhen Graduate School. He received his Bachelor's degree from Tsinghua University in 2000 and PhD from Stevens Institute of Technology in 2006. He worked at Velocyt during 2006–2011 and UES during 2011–2014.



Bo Cao is currently a Ph.D. candidate in Prof Feng Pan's group at Peking University Shenzhen Graduate School, China. He received his B.S. degree in material science from Huazhong University of Science and Technology in 2018. Currently his research interests focus on high energy density cathode materials for lithium batteries, especially on Li-rich and Ni-rich layered oxide materials.



Mingjian Zhang got his Ph.D. degree from Fujian Institute of Research on the Structure of Matter, Chinese Academy of Sciences in 2013, then worked there as an assistant research fellow for one year. From 2014 to 2018, he was a postdoc at School of Advanced Materials, Peking University, and became an assistant research professor since 2018. Meanwhile, he was a research scholar in Brookhaven National Lab from 2016 to 2019, then in the University of Chicago since 2019. He has been engaged in the fields of electrode materials for Li-ion batteries, crystal growth and structure analysis of nonlinear optical crystals.



Shenyang Xu received his B.S. degree from Tiangong University in 2015. Xu is currently a Ph.D. student under the supervision of Prof. Feng Pan at School of Advanced Material, Peking University. His research interests mainly focus on development of functional materials for energy storage.



Feng Pan, founding Dean of School of Advanced Materials, Peking University Shenzhen Graduate School, got B.S. from Dept. Chemistry, Peking University in 1985 and Ph.D. from Dept. of P&A Chemistry, University of Strathclyde, Glasgow, UK, with "Patrick D. Ritchie Prize" for the best Ph.D. in 1994. With more than a decade experience in large international incorporations, Prof. Pan has been engaged in fundamental research and product development of novel optoelectronic and energy storage materials and devices. As Chief Scientist, Prof. Pan led eight entities in Shenzhen to win 150 million RMB grant for the national new energy vehicles (power battery) innovation project since 2013.



Ni Yang is an engineer at School of Advanced Materials, Peking University Shenzhen Graduate School, China. She has over 10 years' experience in material characterization using wide range of analytical tools including FIB, SEM and TEM. Her research interests mainly focus on the FIB and TEM characterization of battery materials.

1. Introduction

Owing to the rapid population growth, energy shortage has become one of the most urgent problems to be solved. One promising strategy is to use clean energies which is renewable and environmentally friendly to replace fossil fuels [1–3]. Renewable energies like wind and solar are intermittent in nature, and they need to be collected and released using high-efficiency energy storage systems [4]. Lithium ion batteries (LIBs), considering the high energy density and long cycle life, have been widely utilized in electric vehicles (EVs) and consumer electronics like mobile phones and laptop computers [5]. Growing deployment of LIB-powered EVs reduces the emission of CO₂, contributing to the mitigation of global warming. Nevertheless, the extensive application of LIBs, especially in the fields of EVs and grid-level energy storage, continues to demand for a higher energy density [6]. The energy density of LIBs largely depends on the electrode materials, especially the cathode materials. In the past decades, layered LiCoO₂

(LCO), spinel LiMn₂O₄ (LMO), olivine LiFePO₄ (LFP), and LiNi_xMn_yCo_zO₂ (NMC, $x + y + z = 1$) have been the major cathode materials in LIB market [7–17]. The first-generation cathode material is LCO, which was first introduced in 1980 [18]. LCO has a high theoretical capacity (about 274 mA h g⁻¹), although only half of which (140 mA h g⁻¹) could be reversibly utilized during practical cycling [7,8]. The second-generation cathode materials include spinel LMO [19], olivine LFP [20], and layered NMC [21]. LMO has been widely utilized in power tools due to the superb cycling stability and low cost, however, its further development is limited due to the low theoretical capacity (148 mA h g⁻¹) and even lower practical capacity (110 mA h g⁻¹) [9]. LFP cathode has been adopted in EVs in recent years. LFP exhibits a high cycling stability, high rate performance, and superior abuse tolerance due to the unique P-O covalent bond [10]. The low energy density and low tap density restrict LFP cathode from a broader market [11,12]. Compared to LFP cathode, NMC cathode has been applied in EV market more effectively and fruitfully. Ni, Mn, and Co elements work coordina-

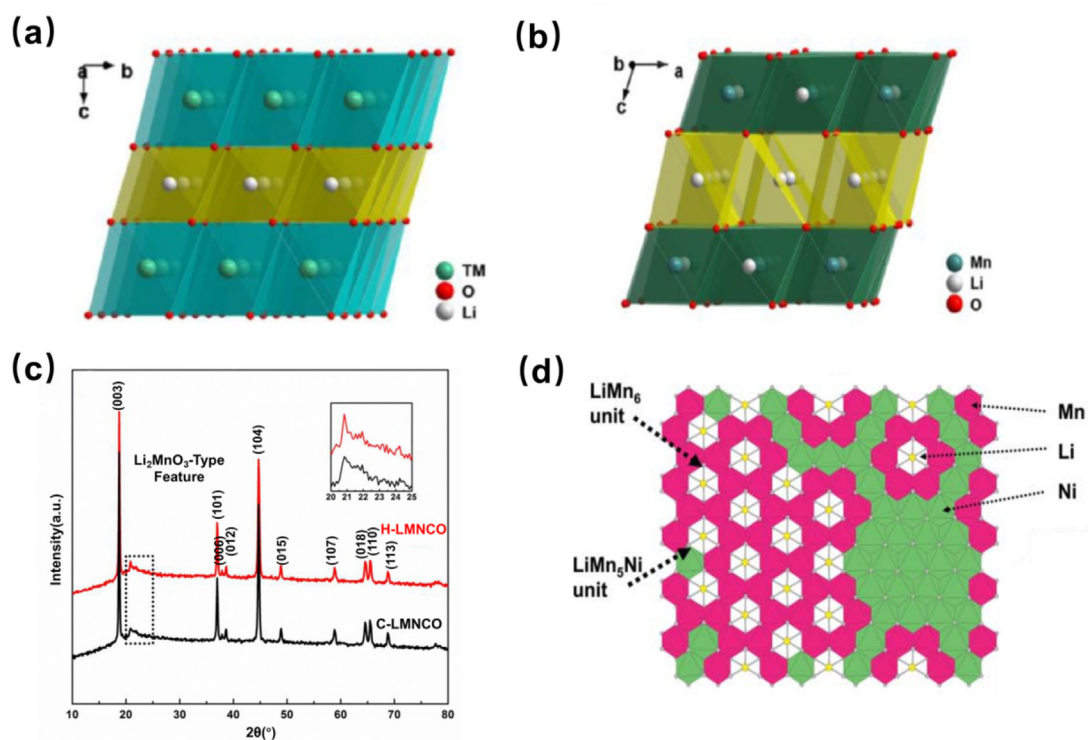


Fig. 1. (a) Crystal structure of trigonal LiMO₂ ($R\bar{3}m$) and (b) monoclinic Li₂MnO₃ ($C2/m$). Reproduced from Ref. [27] with permission from American Chemical Society. (c) XRD patterns of Li_{1.2}Ni_{0.13}Co_{0.13}Mn_{0.54}O_{2.2+δ} synthesized from two different precursors (C for conventional precursor and H for hierarchically structured precursor). Reproduced from Ref. [27] with permission from American Chemical Society. (d) Structural scheme showing the honeycomb pattern consisting of Li@Mn₆ superstructure units in LMR layered oxide. Reproduced from Ref. [29] with permission from Royal Society of Chemistry.

Table 1

Researches about understanding the structure of LMR oxides.

Material	Techniques	Evidence	Model	Ref.
Li _{1.144} Ni _{0.136} Co _{0.136} Mn _{0.544} O ₂	SXRD, SAED	a mixture of LiNi _{1/3} Co _{1/3} Mn _{1/3} O ₂ and Li ₂ MnO ₃ component	composite	[30]
Li _{1.2} Mn _{0.61} Ni _{0.18} Mg _{0.01} O ₂	HAADF-STEM	the slabs are not always stacked in the same way	composite	[31]
Li _{1.2} Fe _{0.4} Mn _{0.4} O ₂	STEM-EELS, NBED, and HRTEM	comprised of Mn-rich nanodomains with the layered rock-salt structure and Fe-rich nanodomains with the cubic rock-salt structure	composite	[32]
Li _{1.2} Cr _{0.4} Mn _{0.4} O ₂	NMR	two characteristic resonances are observed	composite	[33]
Li[Li _{1/9} Ni _{3/9} Mn _{5/9}]O ₂	NMR, EXAFS	two characteristic resonances are observed	composite	[34]
Li _{1.2} Ni _{0.2} Mn _{0.6} O ₂	surface-enhanced Raman spectroscopy	two spectra of Li ₂ MnO ₂ and LiNi _{0.5} Mn _{0.5} O ₂ are observed	composite	[35]
Li _{1.2} Ni _{0.2} Mn _{0.6} O ₂	D - STEM	revealing the absence of $R\bar{3}m$ regions	solid-solution	[36]
Li[Li _{1/3-2x/3} Ni _x Mn _{2/3-x/3}]O ₂	XRD	the superlattice peak positions changed monotonically with Ni content	solid-solution	[37]

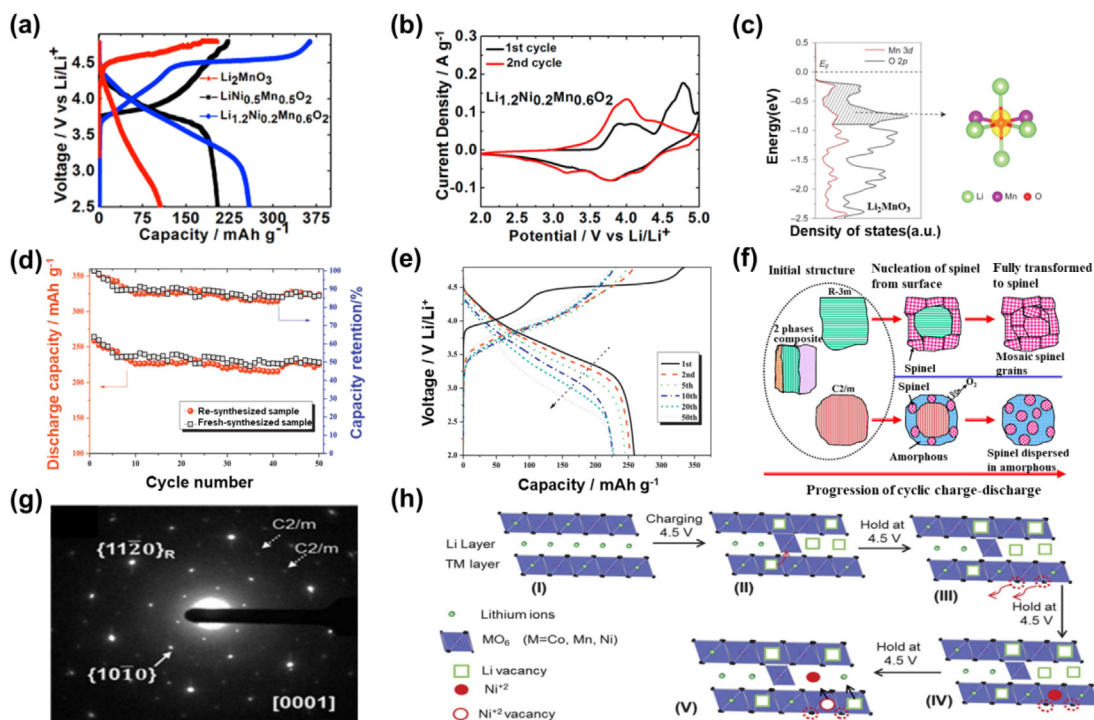


Fig. 2. (a) Initial charging-discharging profiles of Li_2MnO_3 , $\text{LiNi}_{0.5}\text{Mn}_{0.5}\text{O}_2$ and $\text{Li}_{1.2}\text{Ni}_{0.2}\text{Mn}_{0.6}\text{O}_2$. (b) The 1st and 2nd CV curves of $\text{Li}_{1.2}\text{Ni}_{0.2}\text{Mn}_{0.6}\text{O}_2$ in (a). Reproduced from Ref. [35] with permission from American Chemical Society. (c) pDOS of O 2p orbitals and Mn 3d orbitals in Li_2MnO_3 and the corresponding oxygen environment model. Reproduced from Ref. [47] with permission from Springer Nature. (d) Cycling performance of $\text{Li}_{1.2}\text{Ni}_{0.13}\text{Co}_{0.13}\text{Mn}_{0.54}\text{O}_2$ synthesized by two different synthesis methods at 0.1 C in the voltage range of 2.0–4.8 V. (e) The corresponding capacity-voltage profiles of the re-synthesized $\text{Li}_{1.2}\text{Ni}_{0.13}\text{Co}_{0.13}\text{Mn}_{0.54}\text{O}_2$ in (d). Reproduced from Ref. [53] with permission from Elsevier. (f) Schematic representation for the structural transformation of trigonal LiMO_2 component ($R\text{-}3m$) and monoclinic Li_2MnO_3 component ($C2/m$) in $\text{Li}_{1.2}\text{Ni}_{0.1}\text{Mn}_{0.525}\text{Co}_{0.175}\text{O}_2$ during cycling. Reproduced from Ref. [54] with permission from American Chemical Society. (g) Selected area electron diffraction (SAED) pattern obtained along $[0001]$ zone axis of $\text{Li}_{1.2}\text{Co}_{0.1}\text{Mn}_{0.55}\text{Ni}_{0.15}\text{O}_2$ cathode at the charging voltage of 4.5 V. (h) Schematic diagram of TM migration in $\text{Li}_{1.2}\text{Co}_{0.1}\text{Mn}_{0.55}\text{Ni}_{0.15}\text{O}_2$ cathode when holding at 4.5 V. Reproduced from Ref. [55] with permission from Royal Society of Chemistry.

tively in NMC cathode: $\text{Ni}^{2+/3+}$ is responsible for providing capacity, Mn^{4+} is for maintaining the structural stability, and Co^{3+} could promote the diffusion of Li^+ ions [13–16]. However, the traditional NMC cathode only offers limited improvements in terms of practical capacity ($<200 \text{ mA h g}^{-1}$) [17]. The key benchmark for the next-generation cathode material is a higher energy density than all current materials.

Since the report by Dahn et al. in 2001, Li and Mn rich (LMR) layered oxides $x\text{Li}_2\text{MnO}_3 \cdot (1-x)\text{LiMO}_2$ ($M = \text{Mn, Ni, Co, Fe, etc.}$), have been regarded as the next-generation cathode material due to the high specific capacity ($>250 \text{ mA h g}^{-1}$) [22,23]. As depicted in the formula, LMR layered oxides contain two components, trigonal LiMO_2 and monoclinic Li_2MnO_3 . The Li_2MnO_3 component could be activated at the first charging above 4.5 V, providing a high capacity coupling with oxygen redox. In addition, manganese is much cheaper and less toxic than cobalt, which makes LMR oxides more economically attractive compared to LCO [24]. Nevertheless, LMR oxides also have a few of drawbacks. (1) The large irreversible capacity loss during the first cycle, which leads to the low initial Coulombic efficiency. (2) Voltage and capacity decay during cycling. (3) Poor rate performance due to the poor electronic conductivity of manganese-based oxide [9,25,26]. In this review, we focus on these challenges for the commercialization of LMR layered oxides and the recent progress to overcome them. In Section 2, the basic crystal structure and the electrochemical behavior of LMR oxides are introduced. In Section 3, the recent progress on overcoming challenges for LMR layered oxides are summarized. In Section 4, promising developments and future directions for LMR oxides are suggested.

2. Structure and electrochemical performance of LMR cathode

2.1. Crystal structure of LMR oxides

LMR oxides are generally considered as the composite of Li_2MnO_3 and LiMO_2 , therefore the formula could be written as $x\text{Li}_2\text{MnO}_3 \cdot (1-x)\text{LiMO}_2$ ($M = \text{Mn, Ni, Co, Fe, etc.}$). As shown in Fig. 1(a and b) [27], Li_2MnO_3 belongs to monoclinic space group $C2/m$, while LiMO_2 crystallizes in trigonal space group $R\text{-}3m$ [28]. Both of them are constructed by alternately stacking Li layers and transition metal (TM) layers along c axis within the similar cubic close packed oxygen array. The major structural difference of LMR oxides from traditional layered oxides (LCO, NMC, etc.) is the $\text{Li}@Mn_6$ superstructure unit. As shown in Fig. 1(c), a few of peaks could be observed in the range of $20\text{--}25^\circ$ of the X-ray diffractogram (XRD) pattern for LMR oxide, and they cannot be observed in the XRD patterns of traditional layered oxides. This special phenomenon originates from the $\text{Li}@Mn_6$ superstructure unit shown in Fig. 1(d) [29].

Although LMR oxides are composed of trigonal LiMO_2 and monoclinic Li_2MnO_3 , the arrangement of these two structures in LMR oxides is still under debate. We list some researches on understanding the structure of LMR oxides in Table 1. One argument is the composite model, namely, trigonal phase and monoclinic phase co-exist. This model has been proved by many techniques. Qiu et al. proved the co-existence of the two phases in $\text{Li}_{1.144}\text{Ni}_{0.136}\text{Co}_{0.136}\text{Mn}_{0.544}\text{O}_2$ powder by synchrotron X-ray diffractogram (SXRD) [30]. The composite model was also observed in $\text{Li}_{1.2}\text{Mn}_{0.61}\text{Ni}_{0.18}\text{Mg}_{0.01}\text{O}_2$ through high angle annular dark field scanning transmission electron microscopy (HAADF-STEM) [31]. Two

independent Fe and Mn rich nanodomains in $\text{Li}_{1.2}\text{Fe}_{0.4}\text{Mn}_{0.4}\text{O}_2$ were observed by electron energy-loss spectroscopy (EELS) measurements [32]. Besides, the composite model was also supported by Li magic angle spinning (MAS) NMR, extended X-ray absorption fine structure (EXAFS) spectroscopy, and *in situ* surface enhanced Raman spectroscopy [33–35].

Another widely accepted model is the solid-solution model, stating that, single solid-solution phase with $C2/m$ symmetry exists in LMR oxides [36]. It has also been proved through multiple characterization techniques. Jarvis et al. observed single-phase ($C2/m$ symmetry) $\text{Li}_{1.2}\text{Ni}_{0.2}\text{Mn}_{0.6}\text{O}_2$ with ordered Li^+ in TM layer by diffraction scanning TEM (D - STEM) [36]. Shunmugasundaram et al. demonstrated the (020), (110), and (-111) crystallographic planes related with the monoclinic phase in diminished XRD patterns [37].

In summary, there is no unified conclusion about the crystal structure of LMR oxides (composite or solid-solution) till now. One possible reason is that, the actual crystal structure of LMR oxides varies with the elemental compositions (especially the content of lithium) and the synthetic conditions (oxygen partial pressure, cooling rate, etc.) [38,39].

In addition, structure defects are easily introduced during the synthetic process, which affects the electrochemical performance of LMR cathodes to a large extent [40]. Zhang et al. found that the quenching process during the synthesis of Li_2MnO_3 would lead to the formation of Mn^{3+} defects, which have significant impacts on the electrochemical activation and the cycling stability [41]. Chen et al. used molten-salt method to synthesize LMR oxides, and they noticed that there was a Co- and Ni-rich spinel phase with serious anti-site defects on the particle surface, which may be a previously-neglected factor determining the structural stability [42].

2.2. Electrochemical performance of LMR cathodes

The electrochemical performance of cathode materials is closely related to their structures. Since LMR oxides are composed of trigonal LiMO_2 and monoclinic Li_2MnO_3 , the electrochemical property is a combination of the electrochemical behaviors of LiMO_2 and Li_2MnO_3 to some extent. As shown in Fig. 2(a), the charging profile of $\text{Li}_{1.2}\text{Ni}_{0.2}\text{Mn}_{0.6}\text{O}_2$ can be divided into two parts, below 4.5 V and above 4.5 V [35]. It is sloping below 4.5 V, which is similar with that of $\text{LiNi}_{0.5}\text{Mn}_{0.5}\text{O}_2$, indicating the deintercalation of Li^+ from LiMO_2 component and the solid-solution behavior [43,44]. Shimoda et al. proved that this sloping part below 4.5 V was related to TM redox [45]. Above 4.5 V, a long voltage plateau is observed for $\text{Li}_{1.2}\text{Ni}_{0.2}\text{Mn}_{0.6}\text{O}_2$, a behavior similar to Li_2MnO_3 , implying the deintercalation of Li^+ from Li_2MnO_3 component. This voltage plateau only occurs in the first cycle, and disappears in the following cycles. The CV curves of $\text{Li}_{1.2}\text{Ni}_{0.2}\text{Mn}_{0.6}\text{O}_2$ further confirm this phenomenon: a strong oxidation peak occurs around 4.5 V in the first cycle and disappears in the second cycle (Fig. 2b). The long voltage plateau corresponds to the oxygen redox, which could only be found in Li_2MnO_3 and LMR cathodes [46]. The oxygen redox originates from the special Li-O-Li connection in Li_2MnO_3 and LMR oxide, as shown in Fig. 2(c). Compared to Mn, the O $2p$ states contributes more to the total DOS close to the Fermi level (0 to -2.5 eV). Especially, the states within 0 to -0.9 eV originate from the Li-O-Li configuration, which hints that the Li-O-Li configuration is the origin of the oxygen redox chemistry [47]. It has been proved that both of TM redox and oxygen redox could be found during discharging: Ni, Co, and oxygen redox occur in the voltage range of 4.8–3.5 V and Mn redox occurs in the voltage range of 3.5–2.0 V [45].

Although LMR oxides could provide high capacity (>250 mA h g^{-1}) and energy density (>900 Wh kg^{-1}), they also have a few of disadvantages hindering the commercialization. These include: 1)

low initial Coulombic efficiency ($<80\%$); 2) severe capacity and voltage decay during long-term cycling; 3) inferior rate performance compared to that of LCO and NMC cathodes. These challenges are discussed one by one as below.

As shown in Fig. 2(a), about 100 mA h g^{-1} of irreversible capacity could be observed during the first cycle for $\text{Li}_{1.2}\text{Ni}_{0.2}\text{Mn}_{0.6}\text{O}_2$, leading to a low initial Coulombic efficiency of 72.3%, much lower than that of NMC and LCO cathodes. The low initial Coulombic efficiency of LMR cathode is largely attributed to the electrode/electrolyte reaction in the first cycle, especially the oxygen loss. When the charge voltage is below 4.6 V, ethylene carbonate (EC), dimethyl carbonate (DMC) and etc. in the solvent would decompose into CO_2 and other gases due to the oxidizing $\text{O}_2^{\cdot-}$ species at the particle surface. Differential Electrochemical Mass Spectrometry (DEMS) measurements can validate CO_2 release from the surface of the active materials, which could also be observed in other layered cathodes [48]. However, while the charging voltage is higher than 4.7 V, lattice O would evolve in the form of O_2 , leaving vacancies in the structure. These O vacancies lead to the irreversible migration of TM ions to Li sites. Only part of the migrated TM ions can return to their original sites during discharging, which severely decreases the initial Coulombic efficiency of LMR cathode [49]. The form of the oxygen loss has also been debated before. Yin et al. analyzed the evolution of cathode electrolyte interphase (CEI) during the first cycle of the LMR cathode [50]. They found: (1) the reasons of oxygen loss were different for LMR cathodes and Li_2MnO_3 cathode (caused by electrochemical decomposition and chemical decomposition, respectively); (2) the formation/dissolution of CEI was accompanied with Li^+ extraction/insertion; (3) the changes in the valence states of metal ions (Ni, Co, Mn) could accelerate the formation of CEI. Besides, the decomposition of the electrolyte solution at high voltage could not be negligible. The high charging voltage (4.8 V) is normally adopted to obtain high capacity for LMR cathodes by fully utilizing TM redox and oxygen redox. At such a high voltage, the electrolyte normally composed of EC, DMC, and LiPF_6 , would decompose, which accompanies with the surficial side-reaction and the consumption of Li^+ , causing the low initial Coulombic efficiency [51]. Except for the high voltage, the highly oxidizing ions $\text{O}_x^{\cdot-}$, would accelerate the decomposition of LiPF_6 , which accompanies with the generation of HF and PO_xF_y^- [52]. These decomposition products would erode the electrode-electrolyte interphase, resulting in the dissolution of the transition metal ions. Continuous dissolution of the metal ions from the material further leads to a rugged surface and increased interphase impedance, which would cause rapid degradation of the electrode.

The fast capacity and voltage decay of the LMR cathodes during long-term cycling is another issue. As shown in Fig. 2(d), only 85% of the initial discharging capacity is maintained after 50 cycles at 0.1 C for $\text{Li}_{1.2}\text{Ni}_{0.13}\text{Co}_{0.13}\text{Mn}_{0.54}\text{O}_2$. Besides, a severe decay in the discharging voltage could also be observed, as shown in Fig. 2(e) [53]. The decays in both capacity and voltage are largely caused by the structural degradation in the first cycle and the following cycles. Wang et al. proposed a structural degradation model of $\text{Li}_{1.2}\text{Ni}_{0.1}\text{Mn}_{0.525}\text{Co}_{0.175}\text{O}_2$ [54]. As shown in Fig. 2(f), due to the concurrent oxygen and lithium loss from the lattice of Li_2MnO_3 component in the first cycle, the layered structure is destroyed, forming a polycrystalline/amorphous matrix. Different from the Li_2MnO_3 component, the LiMO_2 component evolves to a spinel structure at the surface during the first cycle. The formation of a spinel structure was also observed in $\text{Li}_{1.2}\text{Co}_{0.1}\text{Mn}_{0.55}\text{Ni}_{0.15}\text{O}_2$ during the first charge through selected area electron diffraction (SAED), as shown in Fig. 2(g). The mechanism for the formation of the spinel phase was also proposed. When the voltage is held at 4.5 V, oxygen loss will occur in the form of O_2 , leading to the reduction of $\text{Ni}^{3+}/\text{Ni}^{4+}$ to Ni^{2+} due to the charge compensation. Con-

Table 2

The electrochemical performance of LMR cathodes with different morphology design reported in recent years.

Structure	Reversible capacity (mA h g^{-1})	ICE [a]	Capacity retention	Rate (mA h g^{-1})	Ref.
Nanowires	291 (20 mA g^{-1})	87.7%	91.8% (200 mA g^{-1} after 200 cycles)	135 (2000 mA g^{-1})	[62]
Nanorods	250.9 (20 mA g^{-1})	99.8%	~100% (20 mA g^{-1} after 50 cycles)	121 (1000 mA g^{-1})	[63]
Nanoplates	303 (20 mA g^{-1})	93%	92% (200 mA g^{-1} after 200 cycles)	~180 (1000 mA g^{-1})	[64]
Active crystal growth	230.8 (250 mA g^{-1})	–	95.5% (250 mA g^{-1} after 60 cycles)	141.7 (5000 mA g^{-1})	[65]
3D hollow bowl-shaped	300.9 (20 mA g^{-1})	85%	82% (20 mA g^{-1} after 100 cycles)	103.6 (4000 mA g^{-1})	[66]
3D fusiform-shaped	281.4 (20 mA g^{-1})	–	94% (20 mA g^{-1} after 100 cycles)	166.8 (1000 mA g^{-1})	[67]
3D porous materials	270 (25 mA g^{-1})	–	94.9% (500 mA g^{-1} after 500 cycles)	119.5 (2500 mA g^{-1})	[68]
3D reticular materials	259.14 (20 mA g^{-1})	71.9%	95.6% (200 mA g^{-1} after 50 cycles)	135.7 (1000 mA g^{-1})	[69]
Scaled flake-shaped	242 (20 mA g^{-1})	–	93% (200 mA g^{-1} after 600 cycles)	–	[70]
Hollow microspheres	271 (25 mA g^{-1})	81.6%	87.6% (750 mA g^{-1} after 400 cycles)	132 (2500 mA g^{-1})	[71]
Peanut-shaped	278.3 (20 mA g^{-1})	82.9%	94.2% (200 mA g^{-1} after 100 cycles)	145 (2000 mA g^{-1})	[72]

Notes. [a] ICE denotes initial Coulombic efficiency.

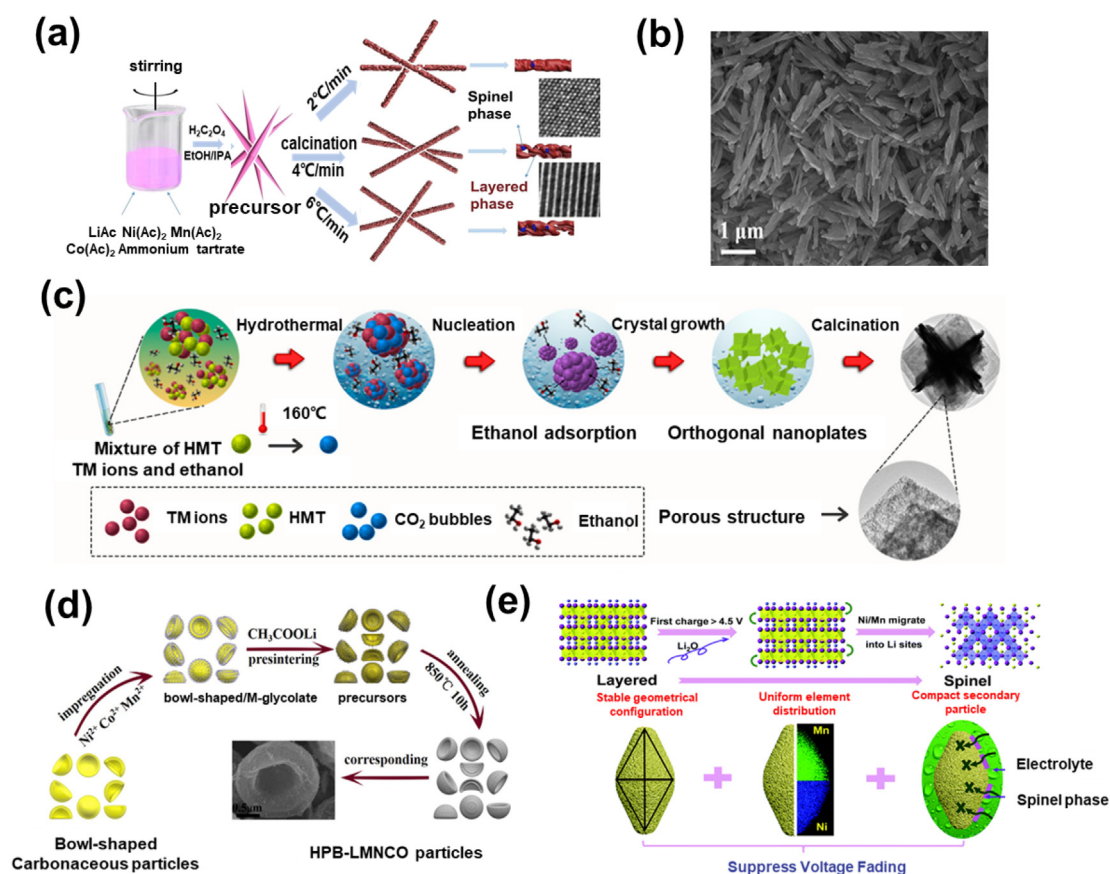


Fig. 3. (a) Schematic illustration of the synthetic process of $\text{Li}_{1.2}\text{Ni}_{0.13}\text{Co}_{0.13}\text{Mn}_{0.54}\text{O}_2$ nanowires. Reproduced from Ref. [62] with permission from Elsevier. (b) Scanning electron microscope (SEM) image of $x\text{Li}_2\text{MnO}_3 \cdot (1-x)\text{LiMnO}_2$ nanorods. Reproduced from Ref. [63] with permission from Elsevier. (c) Schematic illustration of the synthetic process of orthogonally arranged nanoplates. Reproduced from Ref. [64] with permission from American Chemical Society. (d) Scheme of the fabrication process of 3D hollow porous bowl-shaped $\text{Li}_{1.2}\text{Ni}_{0.13}\text{Co}_{0.13}\text{Mn}_{0.54}\text{O}_2$ particles. Reproduced from Ref. [66] with permission from Elsevier. (e) Schematic diagram of the suppression of voltage fading through a preferred orientation (110) plane. Reproduced from Ref. [67] with permission from Royal Society of Chemistry.

sidering the similar ionic radii of Ni^{2+} and Li^+ , Ni^{2+} migrates to the Li layers preferentially compared to other TM cations. Because oxygen loss occurs at the surface, severe cationic mixing would appear at the surface during the first cycle, leading to the formation of a spinel phase, as shown in Fig. 2(h) [55]. The transformation from layered structure to spinel structure in a polycrystalline/amorphous matrix will introduce stress, causing cracks and formation of pores, which are unfavorable for Li^+ (de)intercalation [55]. During long-term cycling, the structural degradation will propagate from the surface to the bulk, resulting in the continuous decay of capacity and voltage. Kang et al. proposed a transition metal migration model in LMR oxides, and they

observed that Li^+ diffusion was much more sluggish during lithiation than during de-lithiation [56]. They thought that, after Li^+ was extracted from Li layers, TM ions would migrate into Li layers, and they could not migrate back to TM layers easily during discharge. However, as more Li^+ intercalate at the end of discharge, the tetrahedral lithium occupancy induced by additional lithiation would facilitate the migration of TM ions back to TM layers, leading to recovery of the layered structure. In addition, Tarascon et al. thought that oxygen redox would come along with Mn migration under 4.6 V during charge [57]. After that, O_2 was released and a structurally-densified single-phase A' formed within the bulk of the materials, not only at the surface. They also found that the

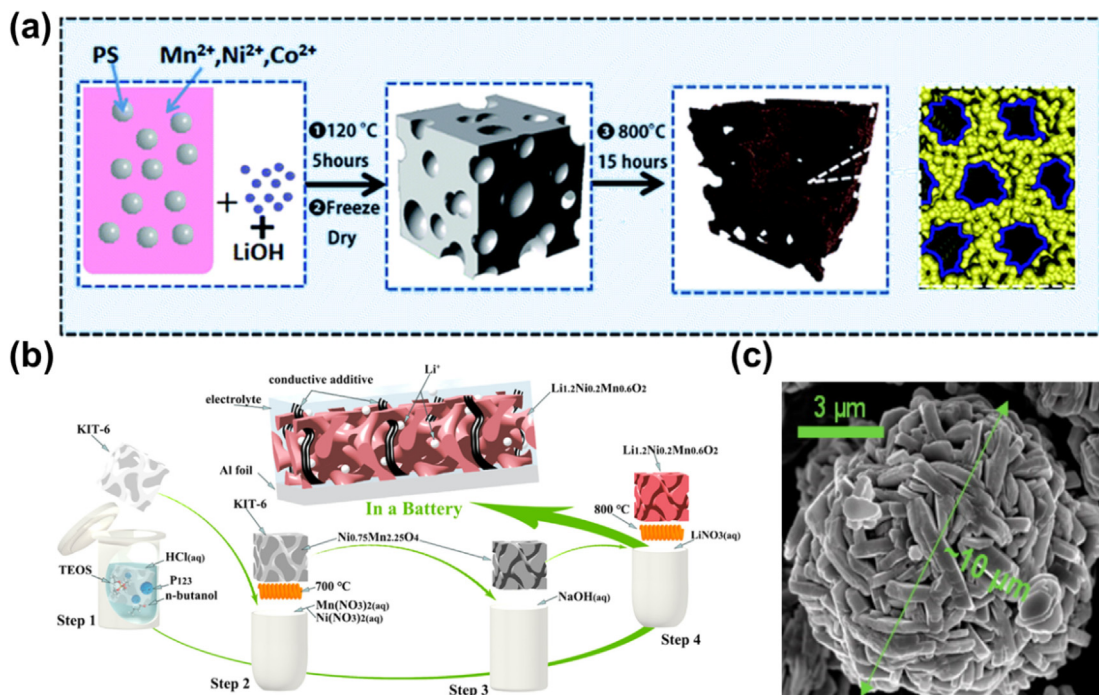


Fig. 4. (a) Schematic illustration of the formation of porous $\text{Li}_{1.2}\text{Ni}_{0.18}\text{Co}_{0.08}\text{Mn}_{0.54}\text{O}_2$. Reproduced from Ref. [68] with permission from Royal Society of Chemistry. (b) Schematic illustration of the synthesizing route for 3D $\text{Li}_{1.2}\text{Ni}_{0.2}\text{Mn}_{0.6}\text{O}_2$ and the morphological evolution. Reproduced from Ref. [69] with permission from American Chemical Society. (c) SEM image of $\text{Li}_{1.2}\text{Ni}_{0.2}\text{Mn}_{0.6}\text{O}_2$ oxide. Reproduced from Ref. [70] with permission from American Chemical Society.

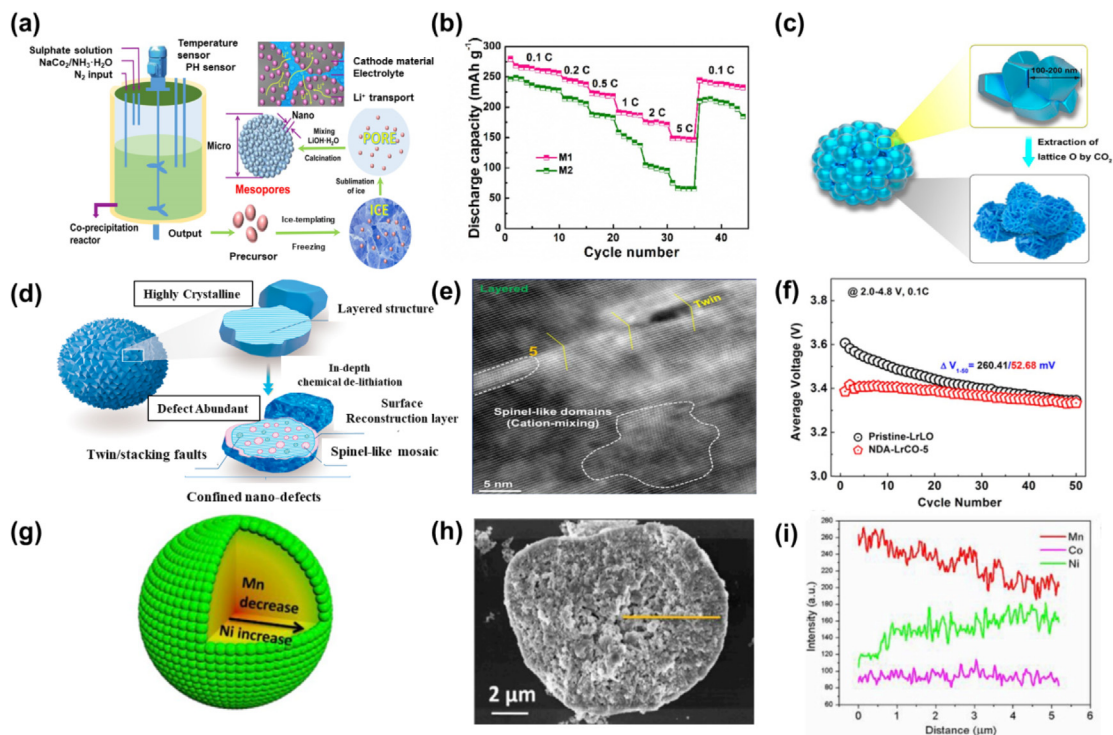


Fig. 5. (a) Schematic illustration of ice-templating coprecipitation method to synthesize $\text{Li}_{1.2}\text{Ni}_{0.2}\text{Mn}_{0.6}\text{O}_2$ with hierarchical mesopore structure. (b) The rate performance of $\text{Li}_{1.2}\text{Ni}_{0.2}\text{Mn}_{0.6}\text{O}_2$ synthesized by freeze drying (M1) and vacuum drying (M2). Reproduced from Ref. [73] with permission from American Chemical Society. (c) Schematic diagram of building nano-porous structures in $\text{Li}_{1.144}\text{Ni}_{0.136}\text{Co}_{0.136}\text{Mn}_{0.544}\text{O}_2$. Reproduced from Ref. [74] with permission from American Chemical Society. (d) Schematic diagram to show various structure defects in $\text{Li}_{1.143}\text{Ni}_{0.136}\text{Co}_{0.136}\text{Mn}_{0.544}\text{O}_2$. (e) TEM image to show nano-defects (stacking faults and cationic mixing) in the $\text{Li}_{1.143}\text{Ni}_{0.136}\text{Co}_{0.136}\text{Mn}_{0.544}\text{O}_2$. (f) Comparison for the average voltage of highly crystalline $\text{Li}_{1.143}\text{Ni}_{0.136}\text{Co}_{0.136}\text{Mn}_{0.544}\text{O}_2$ cathode (Pristine-LrLO) and defect abundant sample (NDA-LrCO-5) during cycling at 0.1 C. Reproduced from Ref. [75] with permission from Elsevier. (g) Schematic diagram of the element gradient distribution in LMR cathodes. (h) SEM image of $\text{Li}_{1.2}\text{Mn}_{0.44}\text{Co}_{0.04}\text{Ni}_{0.32}\text{O}_2$ with element gradient distribution and (i) EDS line scanning along the marked line in (h). Reproduced from Ref. [80] with permission from Elsevier.

capacity loss in the first cycle could be recovered by applying a constant-voltage step during discharge. Li^+ would occupy the tetrahedral sites to form a new P" phase under a harsh reductive condition (<1.4 V), and those Mn ions in Li layers triggered by oxygen redox would serve as "pillars" to stabilize the structure.

Another issue for LMR oxides is the unsatisfactory rate performance. This inferior rate performance can be related to the sluggish dynamics of Mn^{4+} . It has been reported that Mn^{4+} showed slower reaction kinetics in LMR oxides compared to Ni^{2+} and Co^{3+} . Although the Li_2MnO_3 component has been activated in the first charging process, the reaction kinetics of Mn^{4+} is not promoted [25]. On the other hand, the reaction kinetics of Mn^{4+} in LiMO_2 component is also slow, which could be promoted by exchanging Mn^{4+} by Ni^{2+} or Co^{3+} [58]. In addition, elemental segregation of Ni and Co at the particle surface tends to take place during the synthesis process, and it also inhibits the rate performance. These Li^+ diffusion channels within the surface layer are perpendicular to those in the bulk, leading to a virtual barrier in the diffusion path for Li^+ at the surface [59].

3. Recent progress on promoting the electrochemical performance of LMR cathodes

To accelerate the commercialization of LMR cathodes, researchers devoted a lot of efforts to optimize the electrochemical performance through different methods. Fortunately, the three concerns discussed above have been resolved to some extent in recent years. In this section, we will elaborate on these effective methods in three categories: morphology design, bulk design, and surface modification.

3.1. Morphology design

Various morphologies, such as 1D nanowires, 1D nanotubes, 2D nanoplates, 3D porous morphology and other hierarchical nano morphologies, have been widely reported in other layered oxides, including LCO and NMC [60,61]. It is also an effective way to optimize the electrochemical performance of LMR oxides, such as mitigating the capacity and voltage degradation during cycling. The detailed electrochemical performance of LMR cathodes with different morphologies reported in recent years are shown in Table 2.

Cathode materials with nano morphology have better Li^+ diffusion kinetics by shortening the transportation path, thus better rate performance. Deng et al. synthesized $\text{Li}_{1.2}\text{Ni}_{0.13}\text{Co}_{0.13}\text{Mn}_{0.54}\text{O}_2$ spinel/layered nanowires with porous structures *via* a coprecipitation method followed by the controlled calcination steps, as shown in Fig. 3(a) [62]. They found that the content of spinel phase could be easily tuned by changing the heating rate. The nanowires could provide a better connection between the cathode and the electrolyte, which facilitates Li^+ diffusion and restrains the structural degeneration. Thus, the cathode displays a high capacity of 291 mA h g^{-1} at 0.1C and an excellent capacity retention of 91.8% after 200 cycles at 1C. As shown in Fig. 3(b), Yang et al. used hydrothermally synthesized $\beta\text{-MnO}_2$ nanorods as a self-template to fabricate $x\text{Li}_2\text{MnO}_3\text{-(1-x)LiMnO}_2$ nanorods with the diameter of 100–200 nm and the length of 400–1000 nm [63]. Increasing the fraction of Li_2MnO_3 could significantly increase the discharge capacity but lower the cyclic stability, while increasing the fraction of LiMnO_2 could enhance the cyclic stability by suppressing the transformation from layered phase to spinel phase. As shown in Fig. 3(c), Xu et al. constructed $\text{Li}_{1.2}\text{Mn}_{0.52}\text{Ni}_{0.2}\text{Co}_{0.08}\text{O}_2$ oxide with (010)-oriented nanoplates [64]. This novel morphology not only combines the advantages of exposed (010)-planes and the anisotropic Li^+ transport tunnels for fast Li^+ (de)intercalation, but also effectively inhibits the volume expansion during the cycling. The cathode exhibits an initial discharge capacity of 303 mA h g^{-1} with

a Coulombic efficiency of 93%. After 200 cycles at 1C, it still has an excellent capacity retention of 92%. Similarly, Xu et al. synthesized a hierarchical quasi-spherical $\text{Li}_{1.2}\text{Ni}_{0.2}\text{Mn}_{0.6}\text{O}_2$ oxide with active (010)-oriented surface [65]. Combining the hierarchical structure and active (010)-planes, this material exhibits efficient transports of both Li^+ ions and electrons.

In addition, a three-dimensional architecture with more free space between primary particles is another way to improve the cycling stability, since the volume expansion can be accommodated during cycling. Zhang et al. built 3D hollow porous bowl-shaped $\text{Li}_{1.2}\text{Ni}_{0.13}\text{Co}_{0.13}\text{Mn}_{0.54}\text{O}_2$ particles by a soft template method, and the detailed synthetic process is shown in Fig. 3(d) [66]. The material with this unique structure exhibited a high capacity of $300.9 \text{ mA h g}^{-1}$ at the current density of 20 mA g^{-1} . No evident morphological damage could be observed even at a high current density of 400 mA g^{-1} , enabling its superb rate performance. This 3D hollow bowl-shaped architecture facilitates electrolyte penetration, ensuring sufficient contact between the cathode and electrolyte. The packing density was also increased *via* excluding the redundant space. Li et al. designed a three-dimensional fusiform hierarchical micro/nano $\text{Li}_{1.2}\text{Ni}_{0.2}\text{Mn}_{0.6}\text{O}_2$ with preferentially orientated (110) planes through a hydrothermal method (Fig. 3e) [67]. The cathode not only delivered an enhanced rate performance and cycling stability, but also suppressed the voltage decay through the special triangular frame, which could prevent secondary particles from pulverization and ensure the uniform element distribution. The capacity retention achieved 94% after 100 cycles at 0.1C, and no evident voltage decay could be observed. It also delivered a high capacity of $166.8 \text{ mA h g}^{-1}$ at a high rate of 5C. As shown in Fig. 4(a), He et al. used a self-made template to construct a 3D porous $\text{Li}_{1.2}\text{Ni}_{0.18}\text{Co}_{0.08}\text{Mn}_{0.54}\text{O}_2$ cathode with an *in situ* modified surface [68]. This 3D porous structure with a surface modified by carbonaceous compounds, not only increased Li^+ conductivity, but also protected the active material from side reactions with the electrolyte. Thus, the phase transformation from layered to spinel as well as the voltage decay could be suppressed. Li et al. synthesized a 3D reticular $\text{Li}_{1.2}\text{Ni}_{0.2}\text{Mn}_{0.6}\text{O}_2$ cathode material using ordered mesoporous silica as the template [69]. The detailed preparation process and morphological evolution could be seen in Fig. 4(b). This oxide exhibited a high capacity of $195.6 \text{ mA h g}^{-1}$ at 1C with the capacity retention of 95.6% after 50 cycles. The unique morphology of the material provides nanoscale Li^+ pathways, mechanical stability, and easy access for Li^+ to the center of the particle.

Design and construction of special morphologies is also a novel and efficient approach to improve the electrochemical performance of electrode materials. As shown in Fig. 4(c), Oh et al. prepared $\text{Li}_{1.2}\text{Ni}_{0.2}\text{Mn}_{0.6}\text{O}_2$ in 10 μm -sized secondary particles, which were composed of submicron flake-shaped primary particles [70]. The cathode exhibited a high capacity of 242 mA h g^{-1} at 0.1C and displayed a favorable cycling stability with a capacity retention of 93% after 600 cycles at 1C. Similarly, Yu et al. constructed the ball-in-ball hollow $\text{Li}_{1.2}\text{Ni}_{0.13}\text{Co}_{0.13}\text{Mn}_{0.54}\text{O}_2$ microspheres *via* the co-precipitation method by tuning the nucleation, growth, and heterogeneity of the crystals [71]. The cathode showed excellent electrochemical performance with a high capacity of 193 mA h g^{-1} at 3C and a capacity retention of 87.6% after 400 cycles. Zhang et al. fabricated a peanut-like hierarchical micro/nano $\text{Li}_{1.2}\text{Ni}_{0.18}\text{Co}_{0.08}\text{Mn}_{0.54}\text{O}_2$ *via* the solvothermal method [72]. This oxide, with better crystallinity and larger specific surface area than the counterparts, delivered a discharge capacity of $229.9 \text{ mA h g}^{-1}$ at 1C and a capacity retention of 94.2% after 100 cycles.

In summary, the positive effects of nanoscale morphology design can be summarized as below: (1) shortening Li^+ diffusion pathway and increasing rate capacity; (2) releasing the strain from

Table 3

The electrochemical performance of LMR cathodes with different structure designs reported in recent years.

Strategy	Reversible capacity (mA h g ⁻¹)	ICE	Capacity retention	Rate (mA h g ⁻¹)	Ref.
Hierarchical micro/nanostructure	280.1 (20 mA g ⁻¹)	71.05%	85.4% (20 mA g ⁻¹ after 80 cycles)	152.4 (1000 mA g ⁻¹)	[73]
3D micro-/nanostructure	274 (25 mA g ⁻¹)	93.8%	94.8% (25 mA g ⁻¹ after 100 cycles)	197.6 (1250 mA g ⁻¹)	[74]
Structural defects	287 (12.5 mA g ⁻¹)	–	99.2% (25 mA g ⁻¹ after 50 cycles)	150 (750 mA g ⁻¹)	[75]
Stacking faults	310 (20 mA g ⁻¹)	–	69% (20 mA g ⁻¹ after 100 cycles)	–	[76]
Structural defects	187 (25 mA g ⁻¹)	72.8%	~82% (250 mA g ⁻¹ after 300 cycles)	~100 (500 mA g ⁻¹)	[77]
Surface oxygen defects	308.1 (12.5 mA g ⁻¹)	87.3%	89.7% (25 mA g ⁻¹ after 100 cycles)	~80 (250 mA g ⁻¹)	[78]
Li gradient distributions	322.8 (25 mA g ⁻¹)	90.8%	89.2% (50 mA g ⁻¹ after 200 cycles)	–	[79]
Ni/Mn gradient distributions	256.7 (25 mA g ⁻¹)	–	84% (500 mA g ⁻¹ after 100 cycles)	134 (2500 mA g ⁻¹)	[80]
Ni gradient distributions	300 (20 mA g ⁻¹)	90%	74% (20 mA g ⁻¹ after 200 cycles)	156 (2000 mA g ⁻¹)	[81]
Li/Na gradient distributions	277 (25 mA g ⁻¹)	78.4%	92% (125 mA g ⁻¹ after 100 cycles)	112 (2500 mA g ⁻¹)	[82]

Table 4

The electrochemical performance of LMR cathodes with different element doping reported in recent years.

Doping element	Reversible capacity (mA h g ⁻¹)	ICE	Capacity retention	Rate (mA h g ⁻¹)	Ref
Na	307 (30 mA g ⁻¹)	87%	89% (100 mA g ⁻¹ after 100 cycles)	139 (2400 mA g ⁻¹)	[84]
Na	~280 (20 mA g ⁻¹)	–	93.1% (100 mA g ⁻¹ after 200 cycles)	~150 (1000 mA g ⁻¹)	[85]
Na	215.2 (20 mA g ⁻¹)	–	–	130 (1000 mA g ⁻¹)	[87]
Mg	248.6 (20 mA g ⁻¹)	87.9%	94.2 (100 mA g ⁻¹ after 200 cycles)	130 (1000 mA g ⁻¹)	[88]
Mg	206.4 (40 mA g ⁻¹)	62.6%	95.1% (400 mA g ⁻¹ after 100 cycles)	104.4 (1000 mA g ⁻¹)	[89]
Mg	~250 (20 mA g ⁻¹)	80.2%	76% (20 mA g ⁻¹ after 200 cycles)	~120 (1000 mA g ⁻¹)	[90]
Ti	320 (30 mA g ⁻¹)	73.6%	71% (30 mA g ⁻¹ after 300 cycles)	136 (1500 mA g ⁻¹)	[91]
Fe	261 (25 mA g ⁻¹)	84%	94.44% (25 mA g ⁻¹ after 100 cycles)	150 (1000 mA g ⁻¹)	[92]
Ru	280 (20 mA g ⁻¹)	–	98.1% (20 mA g ⁻¹ after 100 cycles)	150 (1000 mA g ⁻¹)	[93]
Na, F	243 (40 mA g ⁻¹)	–	~100% (40 mA g ⁻¹ after 100 cycles)	167 (1000 mA g ⁻¹)	[95]
Co, Mo	297 (12.5 mA g ⁻¹)	86.2%	86.5% (25 mA g ⁻¹ after 50 cycles)	–	[96]
Cd, S	268.5 (25 mA g ⁻¹)	87.2%	90.65% (25 mA g ⁻¹ after 80 cycles)	153.8 (1250 mA g ⁻¹)	[97]
Na, PO ₄ ³⁻	255.7 (25 mA g ⁻¹)	85.69%	93.8% (250 mA g ⁻¹ after 100 cycles)	106.4 (2500 mA g ⁻¹)	[98]

volume change caused by phase transformation, enhancing the mechanical stability, and contributing to the cycling stability. However, there are also some disadvantages using this strategy, such as complicated preparation, high cost, low tap density and etc., which greatly hinder the practical application in scaling up the cathode materials. In addition, it is difficult to achieve consistent morphology in different batches of materials, while even a slight difference in the morphology might lead to a big difference in the performance.

3.2. Bulk design

Bulk design is essential to improve the structural stability so as to promote the electrochemical performance of LMR cathode. This section is divided into two parts: structure design and bulk doping.

3.2.1. Structure design

Structure design is an effective method to enhance the electrochemical performance of LMR cathode, which includes introducing porous structure, structural defects, gradient elemental distribution, and etc.

Firstly, porous structure is an effective strategy to increase the electrolyte/electrode contact area, and buffer the volume expansion due to the phase transformation during cycling. Li et al. designed hierarchical mesoporous structure in Li_{1.2}Ni_{0.2}Mn_{0.6}O₂ through ice-template coprecipitation [73]. As shown in Fig. 5(a and b), the rate performance was promoted notably. For Li_{1.2}Ni_{0.2}Mn_{0.6}O₂ cathode synthesized using a traditional method, the reversible capacity at 1C was only about 56% of the capacity at 0.1C. In contrast, the capacity at 1C has been promoted to 67% of that at 0.1C in the hierarchical mesoporous structure. The mesoporous structure increased Li⁺ diffusion channels, facilitating Li⁺ diffusion at a large current density. A similar method was also utilized by Qiu et al., as shown in Fig. 5(c) [74]. They introduced homogeneous three-dimensional (3D) nano-porous structure in Li_{1.144}Ni_{0.136}Co_{0.136}Mn_{0.544}O₂, which exhibited a micrometer-sized spherical

morphology. It displayed a better rate performance compared to the sample without a porous structure.

Another effective method to improve the electrochemical performance of LMR cathode is introducing structural defects in the lattice. Xia et al. introduced multiple structural defects in Li_{1.143}Ni_{0.136}Co_{0.136}Mn_{0.544}O₂ by well-controlled chemical de-lithiation [75]. As shown in Fig. 5(d and e), these structural defects include twins/stacking faults and spinel-like mosaics in the bulk. Due to the fine pre-rearrangement, the obtained oxide has some characteristics of electrochemically induced hybrid compounds, which could make anion redox more stable. Thus, the defect-rich cathode exhibited superior cycling stability compared to pristine cathode, and the voltage decay was also evidently suppressed (Fig. 5f). Liu et al. also successfully introduced stacking faults in Li_{1.2}Ni_{0.13}Co_{0.13}Mn_{0.54}O₂ through molten salt method [76]. They could control the concentration of stacking faults through tuning the synthetic temperature and the type of molten salt. When the synthetic temperature was 800 °C, the electrochemical performance of Li_{1.2}Ni_{0.13}Co_{0.13}Mn_{0.54}O₂ cathode was the best, and the capacity reached 310 mA h g⁻¹ at 0.1C. The optimal capacity could be attributed to an appropriate amount of stacking faults. Li et al. synthesized Li_{1.2}Ni_{0.2}Mn_{0.6}O₂ with a small amount of structural defects by combining a fast-evaporating approach and a subsequent high temperature calcination [77]. Due to the structural defects, the oxygen loss during the first cycle was reduced, and Mn migration and the phase transformation from layered to spinel were also suppressed. Zhong et al. introduced surface oxygen defects in Li_{1.2}Ni_{0.13}Co_{0.13}Mn_{0.54}O₂ through a facile hydrothermal reaction followed by heat treatment [78]. After the introduction of the oxygen defects, the activity of surface oxygen was reduced, inhibiting the evolution of lattice oxygen in the bulk. Also, surface defects alleviated the lattice microstrain during the delithiation/lithiation process, and enhanced the mechanical property of materials. In addition, the defects induced the formation of spinel structure at the surface, facilitating Li⁺ extraction/insertion so as to promote the rate performance.

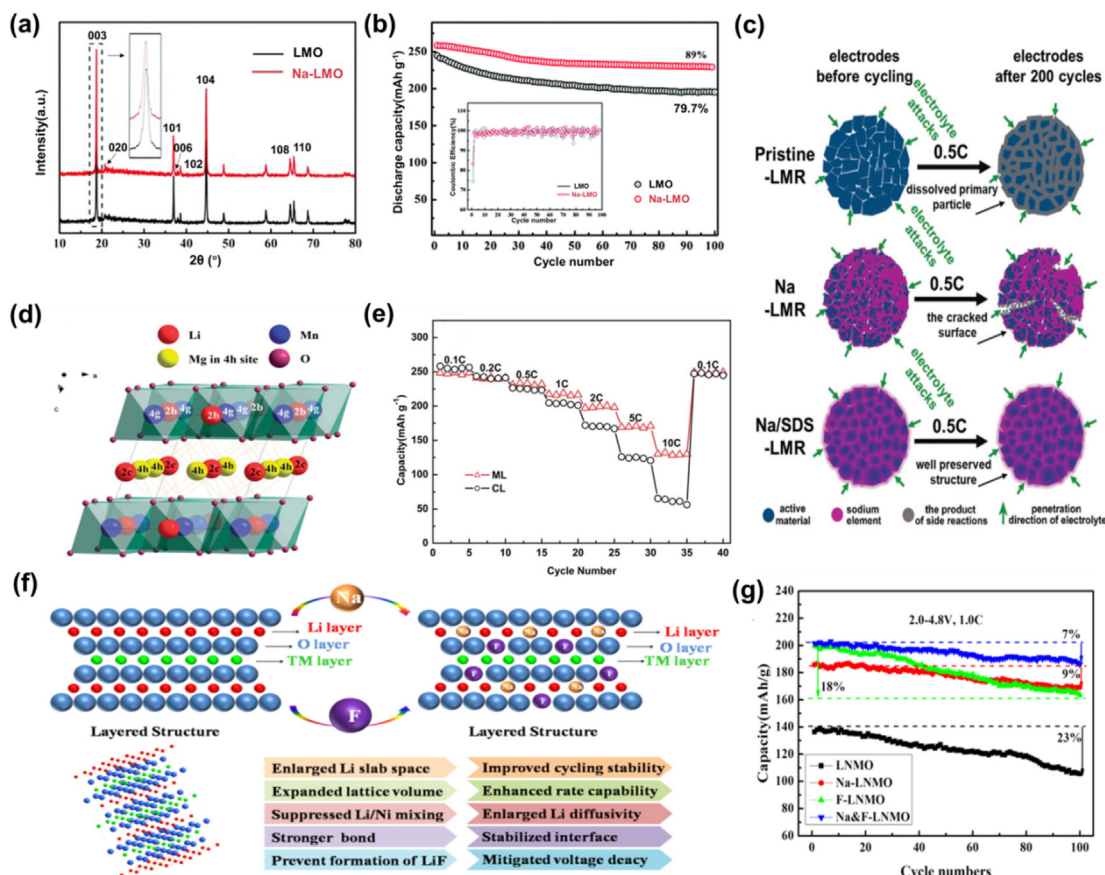


Fig. 6. (a) XRD patterns of $\text{Li}_{1.2}\text{Ni}_{0.13}\text{Co}_{0.13}\text{Mn}_{0.54}\text{O}_2$ and $\text{Li}_{1.17}\text{Na}_{0.03}[\text{Ni}_{0.13}\text{Co}_{0.13}\text{Mn}_{0.54}]\text{O}_2$. (b) The cycling performance of $\text{Li}_{1.2}\text{Ni}_{0.13}\text{Co}_{0.13}\text{Mn}_{0.54}\text{O}_2$ and $\text{Li}_{1.17}\text{Na}_{0.03}[\text{Ni}_{0.13}\text{Co}_{0.13}\text{Mn}_{0.54}]\text{O}_2$ at the current density of 100 mA g^{-1} . Reproduced from Ref. [84] with permission from Royal Society of Chemistry. (c) Schematic diagram of pristine LMR, LMR with surface-doped with Na (Na-LMR) and LMR with homogeneously Na doping (Na/SDS-LMR) before cycling and after 200 cycles. Reproduced from Ref. [85] with permission from Wiley-VCH. (d) Schematic illustration for the structure of Mg-doped $\text{Li}_{1.4}\text{Mg}_{0.1}[\text{Mn}_{0.75}\text{Ni}_{0.25}]\text{O}_{2+\sigma}$. (e) The rate performance of Mg-doped $\text{Li}_{1.4}\text{Mg}_{0.1}[\text{Mn}_{0.75}\text{Ni}_{0.25}]\text{O}_{2+\sigma}$. Reproduced from Ref. [88] with permission from Royal Society of Chemistry. (f) Schematic diagram of Na and F co-doping in $\text{Li}_{1.2}\text{Ni}_{0.2}\text{Mn}_{0.6}\text{O}_2$ cathode. (g) The cycling performance of $\text{Li}_{1.2}\text{Ni}_{0.2}\text{Mn}_{0.6}\text{O}_2$ cathode (LNMO), Na doped LNMO cathode (Na-LNMO), F doped LNMO cathode (F-LNMO) and Na and F co-doped LNMO cathode (Na&F-LNMO) at 0.1 C in the voltage range of 2.0–4.8 V. Reproduced from Ref. [95] with permission from Elsevier.

Table 5

The electrochemical performance of LMR cathodes with different surface coatings reported in recent years.

Strategy	Reversible capacity (mA h g^{-1})	ICE	Capacity retention	Rate(mA h g^{-1})	Ref.
Al_2O_3 coating	268.2(20 mA g^{-1})	-	98% (200 mA g^{-1} after 100 cycles)	-	[102]
SnO_2 coating	264.6(30 mA g^{-1})	-	89.9% (300 mA g^{-1} after 200 cycles)	~125(1000 mA g^{-1})	[103]
AlPO_4 coating	261.9(25 mA g^{-1})	85.2%	-	-	[104]
AlPO_4 coating	267.2(20 mA g^{-1})	78.9%	74.4% (20 mA g^{-1} after 50 cycles)	120.2(2000 mA g^{-1})	[105]
AlPO_4 coating	282.1(30 mA g^{-1})	-	89% (30 mA g^{-1} after 35 cycles)	162.7(1200 mA g^{-1})	[106]
Li_3PO_4 coating	240(25 mA g^{-1})	-	90% (250 mA g^{-1} after 50 cycles)	106(1250 mA g^{-1})	[107]
Li_3PO_4 coating	226.1(20 mA g^{-1})	78.78%	78% (25 mA g^{-1} after 100 cycles)	118(1000 mA g^{-1})	[108]
polyimide coating	269.8(20 mA g^{-1})	-	90.6% (20 mA g^{-1} after 50 cycles)	191.5(400 mA g^{-1})	[109]
LiAlF_4 coating	246 (35 mA g^{-1})	-	92.8% (35 mA g^{-1} after 100 cycles)	133(1750 mA g^{-1})	[110]
AlF_3 coating	~250(25 mA g^{-1})	80.6%	~100% (1/3C after 100 cycles)	-	[111]
Spinel coating	240(30 mA g^{-1})	79.4%	89.1% (150 mA g^{-1} after 200 cycles)	100.9(1000 mA g^{-1})	[112]
spinel coating	211.73(25 mA g^{-1})	-	74.64% (250 mA g^{-1} after 200 cycles)	104(1250 mA g^{-1})	[114]
Al_2O_3 /polyacene coating	280(20 mA g^{-1})	-	98% (40 mA g^{-1} after 100 cycles)	248(200 mA g^{-1})	[115]
Spinel/carbon coating	312.5(25 mA g^{-1})	89.7%	84.4% (250 mA g^{-1} after 200 cycles)	196.1(1250 mA g^{-1})	[116]
Mg_2TiO_4 coating	319(25 mA g^{-1})	-	81% (500 mA g^{-1} after 700 cycles)	~110(2500 mA g^{-1})	[117]
Graphene coating	313(12.5 mA g^{-1})	>100%	-	125(2500 mA g^{-1})	[118]
MoO_2S_2 coating	~220(100 mA g^{-1})	-	96.5% (100 mA g^{-1} after 100cycles)	110.8(1000 mA g^{-1})	[119]
$\text{Na}_2\text{S}_2\text{O}_8$ surface modification	285(25 mA g^{-1})	93.2%	92.2% (25 mA g^{-1} after 50 cycles)	217(250 mA g^{-1})	[120]
LiTaO_3 surface modification	260.5(37.6 mA g^{-1})	76.8%	80.3% (37.6 mA g^{-1} after 200 cycles)	172.4(1128 mA g^{-1})	[121]

Besides, gradient cathode materials have become a hot topic in recent years [79]. Ju et al. designed a gradient oxide $\text{Li}_{1.2}\text{Mn}_{0.44}\text{Co}_{0.04}\text{Ni}_{0.32}\text{O}_2$ (Fig. 5g), in which Ni element increases and Mn element decreases from the bulk to the surface, which could be proved by Energy dispersive X-ray spectroscopy (EDS) line scan

(Fig. 5h-i) [80]. Owing to the gradient distribution of Ni and Mn elements, the Ni/Mn ratio is much higher at the surface. Therefore, TM migration was suppressed and the voltage and capacity decay during long-term cycling decreased. The method has been extended to other LMR oxides [81,82]. Core-shell structural design

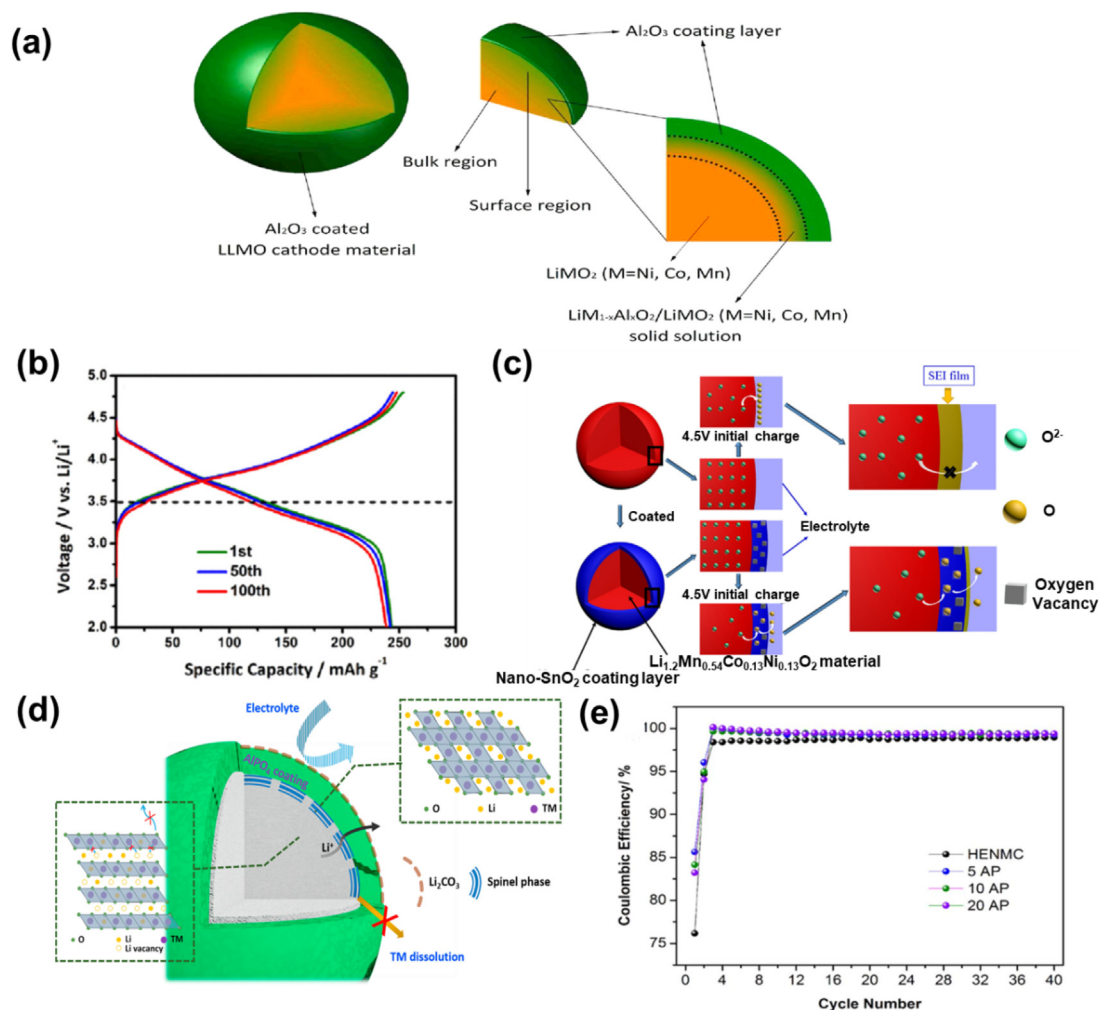


Fig. 7. (a) Schematic diagram of Al_2O_3 coated $\text{Li}_{1.2}\text{Ni}_{0.20}\text{Co}_{0.08}\text{Mn}_{0.52}\text{O}_2$. (b) The capacity-voltage profiles of Al_2O_3 coated $\text{Li}_{1.2}\text{Ni}_{0.20}\text{Co}_{0.08}\text{Mn}_{0.52}\text{O}_2$ in different cycles. Reproduced from Ref. [102] with permission from Elsevier. (c) Schematic illustration of different oxygen migration model in bare and SnO_2 coated $\text{Li}_{1.2}\text{Ni}_{0.13}\text{Co}_{0.13}\text{Mn}_{0.54}\text{O}_2$ (filled with oxygen vacancies at the surface). Reproduced from Ref. [103] with permission from Elsevier. (d) Schematic diagram for the surficial structure of AlPO_4 coated LMR oxide. (e) The Coulombic efficiency of the LMR oxides coated with different ALD cycles of AlPO_4 during long-term cycling. Reproduced from Ref. [104] with permission from Elsevier.

Table 6

The electrochemical performance of LMR cathodes with different surface doping and other surface treatments reported in recent years.

Strategy	Reversible capacity (mA h g^{-1})	ICE	Capacity retention	Rate (mA h g^{-1})	Ref.
Zr doping	211 (25 mA g^{-1})	–	86% (25 mA g^{-1} after 100 cycles)	143 (750 mA g^{-1})	[122]
Al doping	215 (25 mA g^{-1})	67.2%	96% (25 mA g^{-1} after 100 cycles)	~97 (1000 mA g^{-1})	[124]
K doping	282 (25 mA g^{-1})	80.5%	88% (125 mA g^{-1} after 100 cycles)	108 (2500 mA g^{-1})	[125]
Ni doping	257.1 (25 mA g^{-1})	78.6%	89.3% (125 mA g^{-1} after 350 cycles)	169 (1250 mA g^{-1})	[126]
F doping	192.2 (100 mA g^{-1})	–	93.6% (200 mA g^{-1} after 100 cycles)	169.9 (2000 mA g^{-1})	[129]
F doping	227 (36 mA g^{-1})	–	88.1% (36 mA g^{-1} after 50 cycles)	–	[130]
PO_3^{2-} doping	296.7 (30 mA g^{-1})	81.5%	83% (30 mA g^{-1} after 300 cycles)	~160 (1500 mA g^{-1})	[132]
PO_4^{3-} doping	290.1 (20 mA g^{-1})	87.8%	88.2% (100 mA g^{-1} after 400 cycles)	150 (1000 mA g^{-1})	[133]
Surface nitridation	255.5 (30 mA g^{-1})	74.1%	98.3% (30 mA g^{-1} after 75 cycles)	164.7 (1500 mA g^{-1})	[135]

is another effective method to improve the electrochemical performance of LMR oxides. We will elaborate on it in Section 3.3.

In addition, since O3-type LMR cathodes suffer severe voltage and capacity decay, synthesizing O2-type LMR cathodes is also an effective remedy. Xia et al. prepared an O2-type Li-rich material with a single-layer Li_2MnO_3 superstructure via ion exchange [83]. Owing to this novel structure, this oxide could maintain stable oxygen redox reactions and small structural changes during cycling, and delivered an extraordinary reversible capacity of 400 mA h g^{-1} .

In summary, various structure design methods, including introducing porous structure, structural defects, elemental gradient distribution and O2-type structure in LMR cathodes could distinctly promote the electrochemical performance. The detailed electrochemical properties of LMR cathodes with different structure designs reported recently are listed in Table 3. Correspondingly, there are some limitations with them. Porous structure would decrease the tap density of cathode materials, thus the volumetric energy density. Structural defects always require the precise pro-

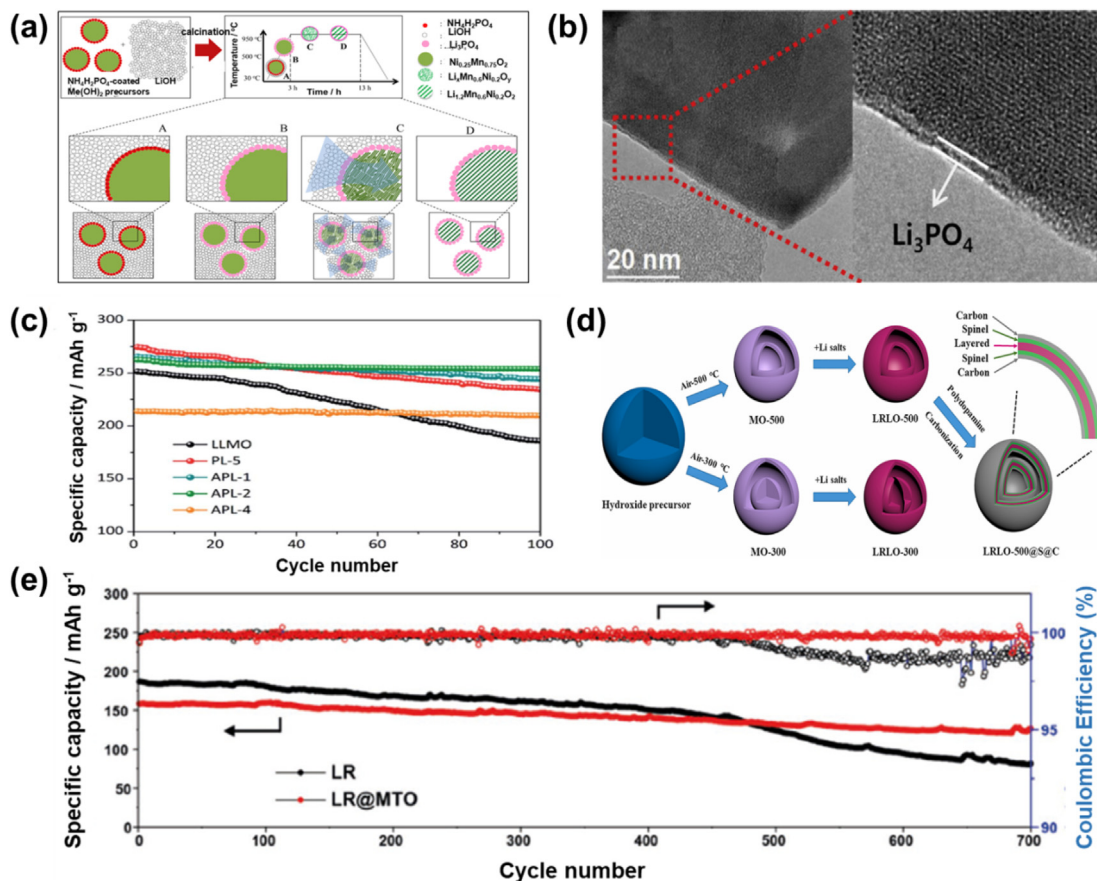


Fig. 8. (a) Illustration of the Li_3PO_4 coating process on the surface of $\text{Li}_{1.2}\text{Ni}_{0.2}\text{Mn}_{0.6}\text{O}_2$ through annealing at different temperatures. (b) TEM image of Li_3PO_4 coating layer. Reproduced from Ref. [107] with permission from Elsevier. (c) The cycling performance of the $\text{Li}_{1.2}\text{Ni}_{0.13}\text{Co}_{0.13}\text{Mn}_{0.54}\text{O}_2$ cathode coated with different contents of Al_2O_3 and polyacene at 0.2 C (APL is short for double-shelled of Al_2O_3 and polyacene, and the number represents different amount of polyacene). Reproduced from Ref. [115] with permission from Royal Society of Chemistry. (d) Schematic diagram of the detailed synthetic process of the LMR cathode coated with a sandwich-like carbon@spinel@layered@spinel@carbon shell. Reproduced from Ref. [116] with permission from Elsevier. (e) Cycle performance of uncoated $\text{Li}_{1.2}\text{Ni}_{0.13}\text{Co}_{0.13}\text{Mn}_{0.54}\text{O}_2$ (LR) and Mg_2TiO_4 coated $\text{Li}_{1.2}\text{Ni}_{0.13}\text{Co}_{0.13}\text{Mn}_{0.54}\text{O}_2$ (LR@MTO) at 2 C. Reproduced from Ref. [117] with permission from John Wiley and Sons.

cess control, and bring with the relative low capacity. Elemental gradient design and ion exchange for O2-type structure also demand complicated synthetic devices, thus increasing the difficulty of commercialization and the production cost a lot.

3.2.2. Bulk doping

Bulk doping has been widely reported as a traditional but effective method to improve the electrochemical performance of cathodes in LIBs, and it has also been widely applied in LMR cathodes (Table 4).

Elements in the third period like Na and Mg, have been widely adopted for bulking doping. He et al. successfully introduced Na ions in the lattice of $\text{Li}_{1.2}\text{Ni}_{0.13}\text{Co}_{0.13}\text{Mn}_{0.54}\text{O}_2$ through a polymer pyrolysis method [84]. Owing to the larger radius of Na^+ , Li slab became thicker while Na^+ replaced Li^+ in Li layers. As shown in Fig. 6(a), (003) peak for $\text{Li}_{1.17}\text{Na}_{0.03}[\text{Ni}_{0.13}\text{Co}_{0.13}\text{Mn}_{0.54}\text{O}_2]$ is located at a lower angle compared to that for $\text{Li}_{1.2}\text{Ni}_{0.13}\text{Co}_{0.13}\text{Mn}_{0.54}\text{O}_2$, implying the increase of Li slab due to Na^+ substitution. Na doping successfully enhanced the structural stability and Li^+ diffusivity. Thus, Na-doped cathode exhibited better cycling stability compared to undoped counterpart, and it retained 89% of the capacity after 100 cycles at the current density of 100 mA g^{-1} (Fig. 6b). He et al. used sodium dodecyl sulfate as a surfactant, and homogeneously introduced Na^+ in the layered lattice of $\text{Li}_{1.2}\text{Ni}_{0.13}\text{Co}_{0.13}\text{Mn}_{0.54}\text{O}_2$, as shown in Fig. 6(c) [85]. Different from the previous reports [86], the introduction of Na^+ caused abundant defects in the form of stacking faults in the lattice. These stacking faults

enhanced the structural stability of $\text{Li}_{1.2}\text{Ni}_{0.13}\text{Co}_{0.13}\text{Mn}_{0.54}\text{O}_2$ cathode, which displayed better cycling stability. Du et al. performed the similar experiments [87]. Interestingly, Na ions have not been introduced to the layered lattice. By contrast, a two-phase composite formed with a new $\text{Na}_{0.7}\text{MnO}_{2.05}$ phase. Li^+ diffused rapidly within the boundaries between these two phases, and composite cathode got superior rate performance (130 mA h g^{-1} at 5 C). Mg doping can also greatly improve electrochemical performance. Yu et al. synthesized a novel cathode material $\text{Li}_{1.4}\text{Mg}_{0.1}[\text{Mn}_{0.75}\text{Ni}_{0.25}]\text{O}_{2+\sigma}$ with uniform Mg doping through coprecipitation and high temperature solid state sintering [88]. They found that, Mg ions were prone to take Li sites (4 h), as shown in Fig. 6(d). The Mg dopant has a distinct effect on promoting Li^+ diffusivity, which evidently improved the rate performance. As shown in Fig. 6(e), $\text{Li}_{1.4}\text{Mg}_{0.1}[\text{Mn}_{0.75}\text{Ni}_{0.25}]\text{O}_{2+\sigma}$ cathode exhibits a discharge capacity of 130 mA h g^{-1} at 10 C, which is much higher than that of $\text{Li}_{1.5}[\text{Mn}_{0.75}\text{Ni}_{0.25}]\text{O}_{2+\sigma}$ cathode. It has also been reported that, the improved cycling stability of LMR cathode by Mg doping could be explained by the reduced charge transfer resistance and the expansion of the unit cell [89,90]. Besides, TM cations are also selected to improve the performance of LMR cathodes, such as Ti, Fe, Ru, etc. [91–94].

In addition, two or more ions together may play different roles in multiple elemental doping, which make it possible for them to work synergistically to produce better electrochemistry than the single elemental doping, namely multi-ion co-doping. Liu et al. doped Na cation and F anion in $\text{Li}_{1.2}\text{Ni}_{0.2}\text{Mn}_{0.6}\text{O}_2$ cathode, as shown

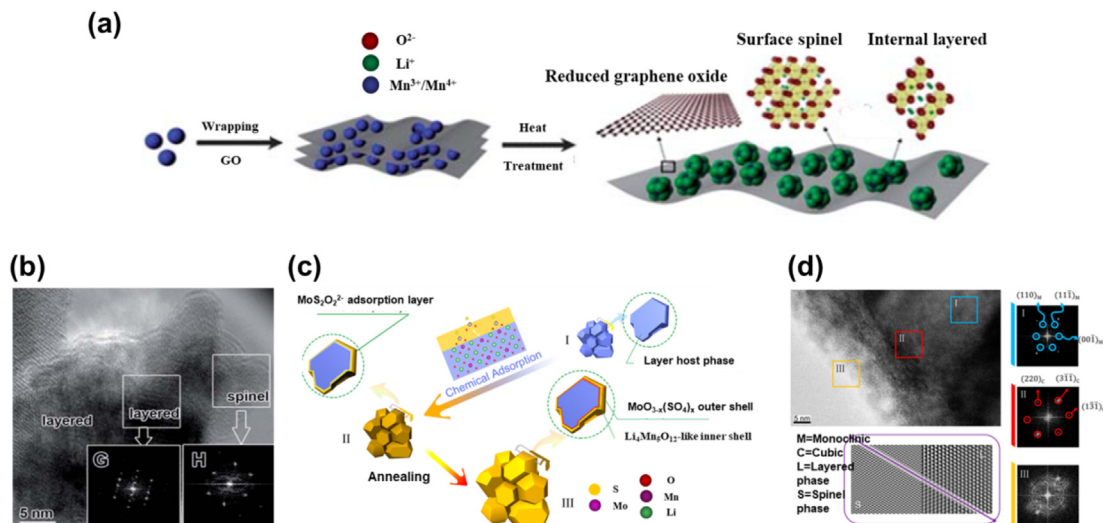


Fig. 9. (a) Schematic illustration of the detailed process of GO modified at the surface of $\text{Li}_{1.2}\text{Ni}_{0.13}\text{Co}_{0.13}\text{Mn}_{0.54}\text{O}_2$ cathode and the following heat treatment. (b) HRTEM image and the corresponding FFT of the layered $\text{Li}_{1.2}\text{Mn}_{0.54}\text{Ni}_{0.13}\text{Co}_{0.13}\text{O}_2$ oxide in the bulk and the spinel structure at the surface after GO modification. Reproduced from Ref. [118] with permission from Royal Society of Chemistry. (c) The synthetic scheme of chemical adsorption to modified MoO_2S_2 at the surface of LMR cathode and the corresponding structure at each step. (d) HRTEM and the corresponding FFT and refined lattice images of the MoO_2S_2 modified LMR cathode. Reproduced from Ref. [119] with permission from American Chemical Society.

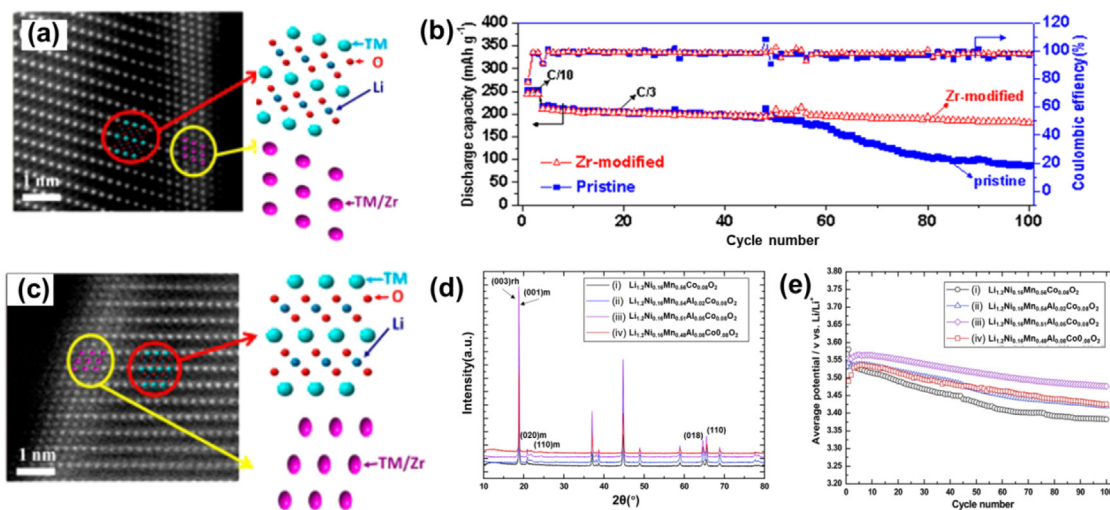


Fig. 10. (a) HAADF-STEM image of the Zr-modified $\text{Li}_{1.2}\text{Ni}_{0.13}\text{Co}_{0.13}\text{Mn}_{0.54}\text{O}_2$ cathode along $[100]$ zone axis and the corresponding atomic models. (b) The cycling performance of Zr-modified $\text{Li}_{1.2}\text{Ni}_{0.13}\text{Co}_{0.13}\text{Mn}_{0.54}\text{O}_2$ cathode and un-modified cathode at C/3. (c) HAADF-STEM image of the Zr-modified $\text{Li}_{1.2}\text{Ni}_{0.13}\text{Co}_{0.13}\text{Mn}_{0.54}\text{O}_2$ cathode after 100 cycles along $[100]$ zone axis and the corresponding atomic models. Reproduced from Ref. [122] with permission from American Chemical Society. (d) XRD patterns of $\text{Li}_{1.2}\text{Ni}_{0.16}\text{Mn}_{0.56}\text{Co}_{0.08}\text{O}_2$ samples doped by different Al contents. (e) The average voltage of the $\text{Li}_{1.2}\text{Ni}_{0.16}\text{Mn}_{0.56}\text{Co}_{0.08}\text{O}_2$ cathode doped by different Al contents during cycling at 0.1 C. Reproduced from Ref. [124] with permission from John Wiley and Sons.

in Fig. 6(f) [95]. The Na and F dopants worked synergistically in the $\text{Li}_{1.2}\text{Ni}_{0.2}\text{Mn}_{0.6}\text{O}_2$ cathode. Na doping partly restricted the forming of spinel structure during cycling, and F doping increased the ionic and electronic conductivity. Thus, co-doped $\text{Li}_{1.12}\text{Na}_{0.08}\text{Ni}_{0.2}\text{Mn}_{0.6}\text{O}_{1.95}\text{F}_{0.05}$ exhibited excellent cycling stability and rate performance, much better than the undoped $\text{Li}_{1.2}\text{Ni}_{0.2}\text{Mn}_{0.6}\text{O}_2$ and the samples only doped by Na or F element alone (Fig. 6g). Cation co-doping has also been reported by Wynn et al [96]. Co and Mo cations co-doped in $\text{Li}_{1.2}\text{Ni}_{0.2}\text{Mn}_{0.6}\text{O}_2$, in which the degradation of capacity and voltage were successfully suppressed during cycling. This could be attributed to the modified distribution of oxygen charge density by Mo doping, which changed the local band structure and impeded the formation of oxygen vacancy, making oxygen redox more reversible. Other co-doping methods for LMR

cathodes like metal ions and nonmetallic ions co-doping have also been reported recently [97,98].

3.3. Surface modification

Surface modification is another effective way to improve the performance of LMR oxides, which includes surface coating, surface doping, and other special surface treatment.

3.3.1. Surface coating

To reduce the side reactions at the electrode/electrolyte interface, it is straightforward to build an electrochemically-inert protective layer, or a surface coating, on the surface of the cathodes [99–101]. For LMR cathodes, metal oxides, phosphate, fluoride,

organic polymer, etc. have been chosen as coating materials, as shown in Table 5.

Al_2O_3 has been widely adopted in LMR cathodes as one of the most popular coating materials due to the material availability and various coating routes. Xu et al. coated highly crystalline Al_2O_3 on $\text{Li}_{1.2}\text{Ni}_{0.20}\text{Co}_{0.08}\text{Mn}_{0.52}\text{O}_2$ through the hydrolysis of aluminum isopropoxide [102]. As shown in Fig. 7(a), three different regions formed from the surface to the bulk: the outer surface region for Al_2O_3 coating layer, the surface region for $\text{LiM}_{1-x}\text{Al}_x\text{O}_2/\text{LiMO}_2$ ($M = \text{Ni, Co, Mn}$) solid solution, and the bulk region for $\text{Li}_{1.2}\text{Ni}_{0.20}\text{Co}_{0.08}\text{Mn}_{0.52}\text{O}_2$. On one hand, Al_2O_3 coating layer reduced the contact area between the electrode and electrolyte, which suppressed cation dissolution to a large extent. On the other hand, the formed $\text{LiM}_{1-x}\text{Al}_x\text{O}_2/\text{LiMO}_2$ hierarchical structure prohibited the phase transformation at the surface. Nearly no capacity or voltage decay was observed in Al_2O_3 coated $\text{Li}_{1.2}\text{Ni}_{0.20}\text{Co}_{0.08}\text{Mn}_{0.52}\text{O}_2$ cathode during long-term cycling (Fig. 7b). Chen et al. successfully coated SnO_2 at the surface of $\text{Li}_{1.2}\text{Ni}_{0.13}\text{Co}_{0.13}\text{Mn}_{0.54}\text{O}_2$ cathode with a uniform thickness of 4–8 nm [103]. The coating layer limited the side reactions between the electrode and electrolyte, producing a thin solid electrolyte interface (SEI) and enhancing the rate performance. In addition, oxygen vacancies were introduced by the SnO_2 coating layer, which was beneficial to oxygen migration in the coating layer (Fig. 7c). Thus, the activation of Li_2MnO_3 in $\text{Li}_{1.2}\text{Ni}_{0.13}\text{Co}_{0.13}\text{Mn}_{0.54}\text{O}_2$ cathode was promoted during the charging-discharging process, increasing the initial capacity.

Phosphates has also been regarded as effective candidates for surface coating. Xiao et al. coated aluminum phosphate (AlPO_4) at the surface of LMR through atomic layer deposition (ALD) method [104]. They found a spinel structure formed at the surface during ALD process, and this spinel layer effectively inhibited the oxygen release during the first charging-discharging, as shown in Fig. 7(d). Therefore, the initial Coulombic efficiency of the LMR cathode was promoted distinctly. When the cathode was coated with 5 ALD cycles of AlPO_4 , it exhibited the best initial Coulombic efficiency (86.2%), as shown in Fig. 7(e). In addition to the pro-

moted initial Coulombic efficiency, AlPO_4 coating was also reported to improve the capacity stability [105,106]. Li_3PO_4 is another phosphate candidate for surface coating. Lee et al. synthesized $\text{Li}_{1.2}\text{Ni}_{0.2}\text{Mn}_{0.6}\text{O}_2$ with a thin Li_3PO_4 coating layer [107]. The coating was prepared during the synthesis of $\text{Li}_{1.2}\text{Ni}_{0.2}\text{Mn}_{0.6}\text{O}_2$, as illustrated in Fig. 8(a). As shown in Fig. 8(b), a thin Li_3PO_4 coating layer could be observed in TEM image, and it enhanced the rate performance of $\text{Li}_{1.2}\text{Ni}_{0.2}\text{Mn}_{0.6}\text{O}_2$. The same coating layer has also been achieved in $\text{Li}_{1.2}\text{Ni}_{0.13}\text{Co}_{0.13}\text{Mn}_{0.54}\text{O}_2$ by polydopamine template method, which enhanced the cycling and rate performance [108].

Surface coating using fluorides, organic polymers, layered and spinel oxides etc. for LMR cathodes, have also been widely reported in recent years [109–113]. Zhang et al. successfully coated AlF_3 at the surface of $\text{Li}_{1.2}\text{Ni}_{0.15}\text{Co}_{0.10}\text{Mn}_{0.55}\text{O}_2$ cathode. The AlF_3 enhanced the structural stability and restricted the formation of the spinel structure at the surface, effectively suppressing the voltage decay during long-term cycling [111]. Pan et al. constructed a $\text{Li}_x\text{TM}_{3-x}\text{O}_4$ -type spinel shell in $\text{Li}_{1.2}\text{Ni}_{0.13}\text{Co}_{0.13}\text{Mn}_{0.54}\text{O}_2$ oxide by *in situ* electrochemical activation [114]. They found that this special spinel coating could slow down the activation of Li_2MnO_3 and alleviate the oxygen loss and Mn dissolution, suppressing the harmful structural degradation. Zhang et al. synthesized $\text{Li}_{1.2}\text{Ni}_{0.13}\text{Co}_{0.13}\text{Mn}_{0.54}\text{O}_2$ with a thin polyimide (PI) layer coated at the surface through polyacrylic acid (PAA) precursor, which improved the cycling stability and rate capability [109]. Multiple-layer coating could combine the function of individual coating layer together. Xu et al. designed a mesoporous Al_2O_3 /polyacene double-shell at the surface of $\text{Li}_{1.2}\text{Ni}_{0.20}\text{Co}_{0.08}\text{Mn}_{0.52}\text{O}_2$. They found that the best electrochemical performance was achieved when the coating was with 5 wt% of polyacene, and 98% of capacity retention could be obtained at 0.2 C after 100 cycles (Fig. 8c) [115]. Peng's group synthesized a sandwich-like carbon@spinel@layered@spinel@carbon shell at the surface of LMR cathode through a facile template-free method (Fig. 8d) [116]. Owing to the special shell structure, the as-prepared sample

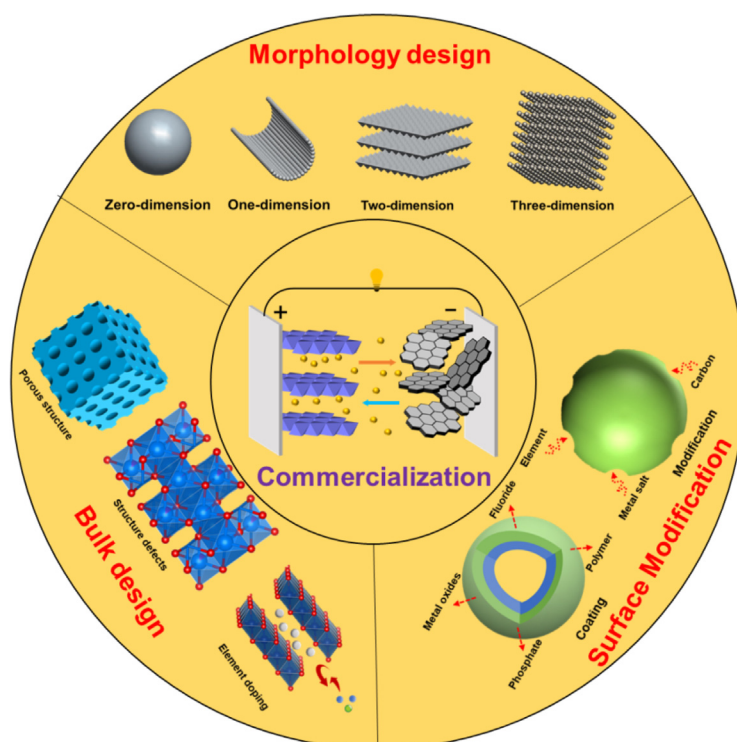


Fig. 11. Schematic illustration for the recent progress in improving the electrochemical performance of LMR cathodes.

delivered a high initial Coulombic efficiency of 89.7% and superb cycling stability, which was demonstrated by a high capacity of 228.3 mA h g⁻¹ after 200 cycles. Chen et al. employed inverse spinel-structured Mg₂TiO₄ coating to suppress oxygen evolution in Li_{1.2}Ni_{0.13}Co_{0.13}Mn_{0.54}O₂ oxide [117]. This dielectric coating, through creating a reverse electric field at the surface, effectively restrained the outward migration of oxygen anions. The high oxygen-affinity elements Mg and Ti could also stabilize the surface oxygen *via* enhancing the energy barrier for the oxygen release. Compared to the unmodified counterpart, the modified electrode showed a superb capacity retention of ~81% after 700 cycles at 2C, as shown in Fig. 8(e).

In addition to these common surface coating, carbon coating or molten salt were also utilized. Carbon coating with a high electric conductivity can improve the electric contact between the particles, thus decreasing the polarization during charging-discharging. Song et al. wrapped graphene oxide (GO) at the surface of sol-gel synthesized Li_{1.2}Ni_{0.13}Co_{0.13}Mn_{0.54}O₂ oxide using a simple chemical approach and subsequent thermal annealing, as shown in Fig. 9(a) [118]. Most interestingly, spinel structure formed at the surface during annealing, which could be observed in HRTEM shown in Fig. 9(b). The modified Li_{1.2}Ni_{0.13}Co_{0.13}Mn_{0.54}O₂ cathode displayed a high discharge capacity of 313 mA h g⁻¹ at the current density of 12.5 mA g⁻¹ and 201 mA h g⁻¹ at the current density of 2500 mA g⁻¹, better than most of the LMR cathodes reported before. The superior rate performance could be attributed to the synergistic effect of the GO coating, the formed spinel structure during annealing, and the recrystallized particles at the surface of the primary particles. Guo et al. used molten MoO₂S₂ to treat the surface of LMR cathode through a novel chemical-adsorption method, and the detailed process is shown in Fig. 9(c) [119]. A continuous and uniform surface modification layer was obtained since Mo-S and Mo-O bonds in MoO₂S₂ could flexibly rotate and well connect with TM cations at the surface. Then, the thiomolybdate adsorption layer induced the formation of a spinel structured layer during subsequent annealing, which could provide extra pathways for Li⁺ and electron diffusion (Fig. 9d). Meanwhile, the MoO_{3-x}(SO₄)_x shell formed after MoO₂S₂ modification, which could suppress the decomposition of electrolyte and inhibit TM dissolution. Therefore, the modified LMR cathode displayed an increased capacity of 225 mA h g⁻¹ at the current density of 100 mA g⁻¹, and showed nearly no capacity decay after 100 cycles. Other molten salt modifications have also been reported in recent years, such as Na₂S₂O₈ and LiTaO₃ [120,121].

Although surface coating is one effective method to promote the electrochemistry, there are still some concerns during practical operations. (1) The uniformity of the coating. A uniform and thorough coating can effectively protect the active materials. Unfortunately, processing routes which can guarantee the uniformity, like ALD, can complicate the synthesis procedures and increase the cost. (2) The thickness of the coating materials. In consideration of the intrinsic inertness, a thick coating may inhibit the electron and Li⁺ transport, and decrease the capacity and rate. (3) The binding force between the coating layer and the active material. The coating layer may fall off due to the volume change of cathode materials during cycling if the binding force is weak. High temperature calcination usually can improve the binding force. In brief, an ideal surface coating is a uniform coating with an optimized thickness and excellent binding force, and it should be implemented through a facile route.

3.3.2. Surface doping

Surface doping is an effective way to improve electron and ion conductivity (Table 6). Li et al. synthesized Li_{1.2}Ni_{0.13}Co_{0.13}Mn_{0.54}O₂ through a coprecipitation method and performed Zr surface doping

using a wet chemical method [122]. They found Zr element distributed within a thickness of 1–2 nm from the surface, and this layer appeared in the form of rock-salt structure, as shown in Fig. 10(a). The modified sample exhibited better cycling stability compared to un-modified one, and it could retain 83% of the initial capacity after 100 cycles at 1/3C, as shown in Fig. 10(b). The promoted cycling properties could be attributed to the rock-salt structure formed at the surface, which could inhibit the formation of spinel phase during the first cycling. As shown in Fig. 10(c), no spinel structure could be observed in the modified Li_{1.2}Ni_{0.13}Co_{0.13}Mn_{0.54}O₂ cathode after 100 cycles. Al doping has been reported as another effective way to promote the performance of LMR cathodes [123]. Nayak et al. doped Li_{1.2}Ni_{0.16}Mn_{0.56}Co_{0.08}O₂ (Fig. 10d) with different contents of Al element and found that Li_{1.2}Ni_{0.16}Mn_{0.51}Al_{0.05}Co_{0.08}O₂ exhibited the best electrochemical performance [124]. The cooperation of Al element at the surface and in the bulk could be accomplished at this ratio, and it not only decreased the impedance but also stabilized the bulk structure. As shown in Fig. 10(e), the voltage decay was also effectively suppressed during long-term cycling. Furthermore, surface modifications of LMR cathodes using nickel and potassium elements have also been reported in previous studies, all of which exhibited better electrochemical performance compared to the unmodified LMR cathodes [125,126].

In addition to cation doping, anion doping is another route for enhancing LMR cathodes. One of the most widely reported doping elements is fluorine, which has also been widely used to dope others layered cathodes [127,128]. Lin et al. found that, after the surface F doping, the cyclic stability was greatly enhanced, delivering a capacity retention of 93.6% after 100 cycles at 1C [129]. Though surface F doping, Yang et al. demonstrated that the formation of vicious LiF in the SEI layer was suppressed, and thus stabilizing the electrode/electrolyte interface [130]. Breddemann et al. successfully doped F element in Li_{1.15}Ni_{0.20}Co_{0.11}Mn_{0.55}O₂ by introducing fluorine gas [131]. They discovered that the rate performance of F-doped LMR cathode was closely related to the F doping content, and it was improved with a low content of F element. This might be attributed to that, the effect of F element only occurred at the surface, and too much F would decrease Li⁺ diffusivity in the bulk. Polyanion doping has also been reported recently, and it could also promote the electrochemical performance of LMR cathode to varied extents [132,133].

3.3.3. Other surface treatments

Erickson et al. synthesized a LMR material with ammonia surface modification [134]. Co and Mn reduction in the bulk and the formation of LiOH, Li₂CO₃, and Li₂O at the surface (due to removal of Li-ion from the bulk) could be observed in the ammonia modified LMR cathode. In addition, the structure rearrangement occurred in the bulk of ammonia modified LMR cathode, and it reduced the coordination number of Co-O and Mn-O bonds, inhibiting the forming of spinel phase. Therefore, the ammonia modified LMR cathode exhibited superior capacity and voltage retention, much better than the un-modified LMR cathode. Similar work has also been reported by Zhang et al., who applied a surface nitridation treatment to Li_{1.17}Ni_{0.25}Mn_{0.58}O₂ [135]. The nitridation treatment was accomplished by heating Li_{1.17}Ni_{0.25}Mn_{0.58}O₂ at 400 °C in the ammonia atmosphere. A trace amount of nitrogen was detected at the surface by XRD, SEM, TEM and X-ray photoelectron spectroscopy (XPS). Owing to the high electrocatalytic activity of nitrogen, the discharge capacity, rate capability, and cycling stability were simultaneously promoted. The modified cathode exhibited a discharge capacity of 255.5 mA h g⁻¹ and nearly no capacity decay was observed after 60 cycles at the current density of 30 mA g⁻¹.

In addition, introducing electrolyte additives to form a protective interface for LMR cathodes is also an effective method. Zheng

et al. utilized the phenyl vinyl sulfone (PVS) as a novel electrolyte additive and the cycling stability of $\text{Li}_{1.2}\text{Ni}_{0.13}\text{Co}_{0.13}\text{Mn}_{0.54}\text{O}_2$ cathode was markedly promoted [136]. This could be attributed to the function of PVS molecule: the aromatic ring enhanced the chemical stability of the interface, and the sulfur enhanced the ionic conductivity. Tan et al. used $(\text{C}_3\text{HF}_6\text{O})_3\text{PO}$ (HFIP) as the electrolyte additive for $\text{Li}_{1.2}\text{Ni}_{0.16}\text{Co}_{0.08}\text{Mn}_{0.56}\text{O}_2$ cathode [137]. HFIP could decompose at the surface of the LMR cathode around 4.2 V (before the decomposition of the solvents) to form a stable CEI layer, which greatly promoted the cycling performance.

It is possible to achieve multiple purposes in one-pass surface treatment, including elemental doping, surface coating, the formation of surficial spinel phase, and etc. The combination of these modifications may lead to better performance than the individual modification mentioned above. However, it is also more difficult to precisely control the effect of each individual medication. Nevertheless, it is normally difficult to ensure a uniform surface after modifications.

4. Conclusion and perspective

In conclusion, LMR layered oxide as one of the most promising next-generation cathodes, still suffers some disadvantages, including the low initial Coulombic efficiency, poor rate performance, and severe voltage and capacity decay. In order to accelerate its commercialization, researchers have developed various effective methods in recent years. We divide these methods into three categories (Fig. 11), and introduce them through various cases in details. Moreover, the issues and limitations for each method are also discussed.

Although a large number of research achievements have been reported, there are still some concerns to be considered before successful commercialization.

1. Although the initial Coulombic efficiency of LMR cathode has been promoted by the modification methods mentioned above, it still cannot meet the requirement for a practical LIB system.

2. The previously reported modification methods can only promote the electrochemical performance of LMR cathode in one or two aspects, which cannot solve all the problems mentioned above. Thus, better modification methods still need to be developed.

3. The processing cost should be considered. Most of the modification methods mentioned above are complex and expensive, and they are not ready for extensive application.

4. It is recommended to improve the performance of LMR cathode from the aspect of the structure unit design, since the electrochemical performance largely depends on the structure units, and little related work is reported.

5. Compared with LCO, LMR cathode has a low tap density due to the polycrystalline morphology consisting of nanosized primary particles. Therefore, the tap density of LMR cathode should be promoted a lot before the commercialization. One effective method to promote the tap density of the layered materials is to synthesize single crystal layered materials, which has been utilized in LCO and Ni-rich NMC cathode [138,139]. The single-crystal layered cathodes can achieve a larger tap density compared to secondary-particle layered cathodes, because the density of a single crystal particle is close to the theoretical value.

Declaration of Competing Interest

The authors declare that they have no known competing financial interests or personal relationships that could have appeared to influence the work reported in this paper.

Acknowledgments

This work was financially supported by the National Key R&D Program of China (2016YFB0700600), the Soft Science Research Project of Guangdong Province (No. 2017B030301013), and the Shenzhen Science and Technology Research Grant (ZDSYS201707281026184).

References

- [1] B. Dunn, H. Kamath, J.M. Tarascon, *Science* 334 (2011) 928–935.
- [2] M.M. Thackeray, C. Wolverton, E.D. Isaacs, *Energy Environ. Sci.* 5 (2012) 7854–7863.
- [3] M.S. Whittingham, *Proc. IEEE* 100 (2012) 1518–1534.
- [4] M.R. Palacin, *Chem. Soc. Rev.* 38 (2009) 2565–2575.
- [5] Y. Nishi, *J. Power Sources* 100 (2001) 101–106.
- [6] J.M. Tarascon, M. Armand, *Nature* 414 (2001) 359–367.
- [7] N.A. Godshall, I.D. Raistrick, R.A. Huggins, *Mater. Res. Bull.* 15 (1980) 561–570.
- [8] G.G. Amatucci, J.M. Tarascon, L.C. Klein, *J. Electrochem. Soc.* 143 (1996) 1114–1123.
- [9] J. Zheng, S. Myeong, W. Cho, P. Yan, J. Xiao, C. Wang, J. Cho, J.-G. Zhang, *Adv. Energy Mater.* 7 (2017) 1601284.
- [10] J. Wang, X. Sun, *Energy Environ. Sci.* 5 (2012) 5163–5185.
- [11] L.-X. Yuan, Z.-H. Wang, W.-X. Zhang, X.-L. Hu, J.-T. Chen, Y.-H. Huang, J.B. Goodenough, *Energy Environ. Sci.* 4 (2011) 269–284.
- [12] Y. Wu, S. Chong, Y. Liu, S. Guo, L. Bai, C. Li, *Chinese J. Struct. Chem.* 37 (2018) 2011–2023.
- [13] T. Ohzuku, Y. Makimura, *Chem. Lett.* (2001) 744–745.
- [14] B.J. Hwang, Y.W. Tsai, D. Carlier, G. Ceder, *Chem. Mater.* 15 (2003) 3676–3682.
- [15] J. Hu, J. Zhang, *Chinese J. Struct. Chem.* 38 (2019) 2005–2008.
- [16] Y. Wei, J.X. Zheng, S.H. Cui, X.H. Song, Y.T. Su, W.J. Deng, Z.Z. Wu, X.W. Wang, W.D. Wang, M.M. Rao, Y. Lin, C.M. Wang, K. Amine, F. Pan, *J. Am. Chem. Soc.* 137 (2015) 8364–8367.
- [17] H.J. Noh, S. Yoon, C.S. Yoon, Y.K. Sun, *J. Power Sources* 233 (2013) 121–130.
- [18] K. Mizushima, P.C. Jones, P.J. Wiseman, J.B. Goodenough, *Mater. Res. Bull.* 15 (1980) 783–789.
- [19] M.M. Thackeray, W.I.F. David, P.G. Bruce, J.B. Goodenough, *Mater. Res. Bull.* 18 (1983) 461–472.
- [20] A.K. Padhi, K.S. Nanjundaswamy, J.B. Goodenough, *J. Electrochem. Soc.* 144 (1997) 1188–1194.
- [21] M. Yoshio, H. Noguchi, J. Itoh, M. Okada, T. Mouri, *J. Power Sources* 90 (2000) 176–181.
- [22] Z.H. Lu, L.Y. Beaulieu, R.A. Donabarger, C.L. Thomas, J.R. Dahn, *J. Electrochem. Soc.* 149 (2002) A778–A791.
- [23] M.M. Thackeray, C.S. Johnson, J.T. Vaughey, N. Li, S.A. Hackney, *J. Mater. Chem.* 15 (2005) 2257–2267.
- [24] C. Zhan, T. Wu, J. Lu, K. Amine, *Energy Environ. Sci.* 11 (2018) 243–257.
- [25] X. Yu, Y. Lyu, L. Gu, H. Wu, S.-M. Bak, Y. Zhou, K. Amine, S.N. Ehrlich, H. Li, K.-W. Nam, X.-Q. Yang, *Adv. Energy Mater.* 4 (2014) 1300950.
- [26] R. Shunmugasundaram, R.S. Arumugam, J.R. Dahn, *Chem. Mater.* 27 (2015) 757–767.
- [27] R. Yu, X. Zhang, T. Liu, X. Xu, Y. Huang, G. Wang, X. Wang, H. Shu, X. Yang, *ACS Sustainable Chem. Eng.* 5 (2017) 8970–8981.
- [28] J. Hong, H. Gwon, S.-K. Jung, K. Ku, K. Kang, *J. Electrochem. Soc.* 162 (2015) A2447–A2467.
- [29] M.M. Thackeray, S.-H. Kang, C.S. Johnson, J.T. Vaughey, R. Benedek, S.A. Hackney, *J. Mater. Chem.* 17 (2007) 3112–3125.
- [30] B. Qiu, J. Wang, Y. Xia, Z. Wei, S. Han, Z. Liu, *J. Power Sources* 268 (2014) 517–521.
- [31] A. Boulineau, L. Simonin, J.-F. Colin, E. Canevet, L. Daniel, S. Patoux, *Chem. Mater.* 24 (2012) 3558–3566.
- [32] J. Kikkawa, T. Akita, M. Tabuchi, M. Shikano, K. Tatsumi, M. Kohyama, *J. Appl. Phys.* 103 (2008).
- [33] C.J. Pan, Y.J. Lee, B. Ammundsen, C.P. Grey, *Chem. Mater.* 14 (2002) 2289–2299.
- [34] W.S. Yoon, N. Kim, X.Q. Yang, J. McBreen, C.P. Grey, *J. Power Sources* 119 (2003) 649–653.
- [35] S. Hy, F. Felix, J. Rick, W.-N. Su, B.J. Hwang, *J. Am. Chem. Soc.* 136 (2014) 999–1007.
- [36] K.A. Jarvis, Z. Deng, L.F. Allard, A. Manthiram, P.J. Ferreira, *Chem. Mater.* 23 (2011) 3614–3621.
- [37] R. Shunmugasundaram, R.S. Arumugam, J.R. Dahn, *J. Electrochem. Soc.* 163 (2016) A1394–A1400.
- [38] E. McCalla, C.M. Lowartz, C.R. Brown, J.R. Dahn, *Chem. Mater.* 25 (2013) 912–918.
- [39] K.A. Jarvis, C.-C. Wang, A. Manthiram, P.J. Ferreira, *J. Mater. Chem. A* 2 (2014) 1353–1362.
- [40] C. Genevois, H. Koga, L. Croguennec, M. Menetrier, C. Delmas, F. Weill, *J. Phys. Chem. C* 119 (2015) 75–83.
- [41] L. Xiao, J. Xiao, X. Yu, P. Yan, J. Zheng, M. Engelhard, P. Bhattacharya, C. Wang, X.-Q. Yang, J.-G. Zhang, *Nano Energy* 16 (2015) 143–151.

- [42] A.K. Shukla, Q.M. Ramasse, C. Ophus, H. Duncan, F. Hage, G. Chen, *Nat. Commun.* 6 (2015) 8711.
- [43] J. Wang, X. He, E. Paillard, N. Laszczynski, J. Li, S. Passerini, *Adv. Energy Mater.* 6 (2016) 1600906.
- [44] Z.H. Lu, J.R. Dahn, *J. Electrochem. Soc.* 149 (2002) A815–A822.
- [45] K. Shimoda, T. Minato, K. Nakanishi, H. Komatsu, T. Matsunaga, H. Tanida, H. Arai, Y. Ukyo, Y. Uchimoto, Z. Ogumi, *J. Mater. Chem. A* 4 (2016) 5909–5916.
- [46] C.S. Johnson, J.S. Kim, C. Lefief, N. Li, J.T. Vaughey, M.M. Thackeray, *Electrochem. Commun.* 6 (2004) 1085–1091.
- [47] D.-H. Seo, J. Lee, A. Urban, R. Malik, S. Kang, G. Ceder, *Nat. Chem.* 8 (2016) 692–697.
- [48] A.T.S. Freiberg, J. Sickingler, S. Solchenbach, H.A. Gasteiger, *Electrochim. Acta* 346 (2020) 136271.
- [49] P.K. Nayak, E.M. Erickson, F. Schipper, T.R. Penki, N. Munichandraiah, P. Adelhelm, H. Sclar, F. Amalraj, B. Markovsky, D. Aurbach, *Adv. Energy Mater.* 8 (2018) 1702397.
- [50] Z.-W. Yin, X.-X. Peng, J.-T. Li, C.-H. Shen, Y.-P. Deng, Z.-G. Wu, T. Zhang, Q.-B. Zhang, Y.-X. Mo, K. Wang, L. Huang, H. Zheng, S.-G. Sun, *ACS Appl. Mater. Interfaces* 11 (2019) 16214–16222.
- [51] K.-W. Nam, S.-M. Bak, E. Hu, X. Yu, Y. Zhou, X. Wang, L. Wu, Y. Zhu, K.-Y. Chung, X.-Q. Yang, *Adv. Funct. Mater.* 23 (2013) 1047–1063.
- [52] F. Wu, W. Li, L. Chen, Y. Su, L. Bao, W. Bao, Z. Yang, J. Wang, Y. Lu, S. Chen, *Energy Storage Mater.* 28 (2020) 383–392.
- [53] L. Li, X. Zhang, R. Chen, T. Zhao, J. Lu, F. Wu, K. Amine, *J. Power Sources* 249 (2014) 28–34.
- [54] M. Gu, I. Belharouak, J. Zheng, H. Wu, J. Xiao, A. Genc, K. Amine, S. Thevuthasan, D.R. Baer, J.-G. Zhang, N.D. Browning, J. Liu, C. Wang, *ACS Nano* 7 (2013) 760–767.
- [55] D. Mohanty, A.S. Sefat, S. Kalnaus, J. Li, R.A. Meisner, E.A. Payzant, D.P. Abraham, D.L. Wood, C. Daniel, *J. Mater. Chem. A* 1 (2013) 6249–6261.
- [56] K. Ku, B. Kim, S.-K. Jung, Y. Gong, D. Eum, G. Yoon, K.-Y. Park, J. Hong, S.-P. Cho, N. Kim, H. Kim, E. Jeong, L. Gu, K. Kang, *Energy Environ. Sci.* 13 (2020) 1269–1278.
- [57] E. Yin, A. Grimaud, G. Rousse, A.M. Abakumov, A. Senyshyn, L. Zhang, S. Trabesinger, A. Iadecola, D. Foix, D. Giaume, J.-M. Tarascon, *Nat. Commun.* 11 (2020) 1252.
- [58] M.N. Ates, S. Mukerjee, K.M. Abraham, *J. Electrochem. Soc.* 161 (2014) A355–A363.
- [59] M. Gu, I. Belharouak, A. Genc, Z. Wang, D. Wang, K. Amine, F. Gao, G. Zhou, S. Thevuthasan, D.R. Baer, J.-G. Zhang, N.D. Browning, J. Liu, C. Wang, *Nano Lett.* 12 (2012) 5186–5191.
- [60] Y.-K. Sun, Z. Chen, H.-J. Noh, D.-J. Lee, H.-G. Jung, Y. Ren, S. Wang, C.S. Yoon, S.-T. Myung, K. Amine, *Nat. Mater.* 11 (2012) 942–947.
- [61] Q. Wu, W.R. Li, Y. Cheng, Z.Y. Jiang, *Mater. Chem. Phys.* 91 (2005) 463–467.
- [62] B. Deng, Y. Chen, P. Wu, J. Han, Y. Li, H. Zheng, Q. Xie, L. Wang, D.-L. Peng, *J. Power Sources* 418 (2019) 122–129.
- [63] F. Yang, Q. Zhang, X. Hu, T. Peng, J. Liu, *J. Power Sources* 353 (2017) 323–332.
- [64] M. Xu, L. Fei, W. Zhang, T. Li, W. Lu, N. Zhang, Y. Lai, Z. Zhang, J. Fang, K. Zhang, J. Li, H. Huang, *Nano Lett.* 17 (2017) 1670–1677.
- [65] L. Chen, Y. Su, S. Chen, N. Li, L. Bao, W. Li, Z. Wang, M. Wang, F. Wu, *Adv. Mater.* 26 (2014) 6756–6760.
- [66] Y. Zhang, W. Zhang, S. Shen, X. Yan, A. Wu, J. Yin, J. Zhang, *J. Power Sources* 380 (2018) 164–173.
- [67] Y. Li, Y. Bai, C. Wu, J. Qian, G. Chen, L. Liu, H. Wang, X. Zhou, F. Wu, *J. Mater. Chem. A* 4 (2016) 5942–5951.
- [68] X. He, J. Wang, R. Wang, B. Qiu, H. Frielinghaus, P. Niehoff, H. Liu, M.C. Stan, E. Paillard, M. Winter, J. Li, *J. Mater. Chem. A* 4 (2016) 7230–7237.
- [69] L. Li, L. Wang, X. Zhang, Q. Xue, L. Wei, F. Wu, R. Chen, *ACS Appl. Mater. Interfaces* 9 (2017) 1516–1523.
- [70] P. Oh, S. Myeong, W. Cho, M.J. Lee, M. Ko, H.Y. Jeong, J. Cho, *Nano Lett.* 14 (2014) 5965–5972.
- [71] F.-D. Yu, L.-F. Que, Z.-B. Wang, Y. Xue, Y. Zhang, B.-S. Liu, D.-M. Gu, *J. Mater. Chem. A* 5 (2017) 9365–9376.
- [72] Y.-D. Zhang, Y. Li, X.-Q. Niu, D.-H. Wang, D. Zhou, X.-L. Wang, C.-D. Gu, J.-P. Tu, *J. Mater. Chem. A* 3 (2015) 14291–14297.
- [73] Y. Li, C. Wu, Y. Bai, L. Liu, H. Wang, F. Wu, N. Zhang, Y. Zou, *ACS Appl. Mater. Interfaces* 8 (2016) 18832–18840.
- [74] B. Qiu, C. Yin, Y. Xia, Z. Liu, *ACS Appl. Mater. Interfaces* 9 (2017) 3661–3666.
- [75] H. Guo, Z. Wei, K. Jia, B. Qiu, C. Yin, F. Meng, Q. Zhang, L. Gu, S. Han, Y. Liu, H. Zhao, W. Jiang, H. Cui, Y. Xia, Z. Liu, *Energy Storage Mater.* 16 (2019) 220–227.
- [76] J. Liu, M. Hou, J. Yi, S. Guo, C. Wang, Y. Xia, *Energy Environ. Sci.* 7 (2014) 705–714.
- [77] X. Xiang, W. Li, *J. Solid State Electrochem.* 19 (2015) 221–227.
- [78] J. Zhong, Z. Yang, Y. Liu, J. Li, X. Wang, F. Kang, *Electrochim. Acta* 328 (2019) 134987.
- [79] Z. Zhu, D. Yu, Y. Yang, C. Su, Y. Huang, Y. Dong, I. Waluyo, B. Wang, A. Hunt, X. Yao, J. Lee, W. Xue, J. Li, *Nat. Energy* 4 (2019) 1049–1058.
- [80] X. Ju, X. Hou, Z. Liu, H. Zheng, H. Huang, B. Qu, T. Wang, Q. Li, J. Li, *J. Power Sources* 437 (2019) 226902.
- [81] B. Wu, X. Yang, X. Jiang, Y. Zhang, H. Shu, P. Gao, L. Liu, X. Wang, *Adv. Funct. Mater.* 28 (2018) 1803392.
- [82] X. Ding, Y.-X. Li, S. Wang, J.-M. Dong, A. Yasmin, Q. Hu, Z.-Y. Wen, C.-H. Chen, *Nano Energy* 61 (2019) 411–419.
- [83] Y. Zuo, B. Li, N. Jiang, W. Chu, H. Zhang, R. Zou, D. Xia, *Adv. Mater.* 30 (2018) 1707255.
- [84] W. He, D. Yuan, J. Qian, X. Ai, H. Yang, Y. Cao, *J. Mater. Chem. A* 1 (2013) 11397–11403.
- [85] W. He, P. Liu, B. Qu, Z. Zheng, H. Zheng, P. Deng, P. Li, S. Li, H. Huang, L. Wang, Q. Xie, D.-L. Peng, *Adv. Sci.* 6 (2019) 1802114.
- [86] M. Lengyel, K.-Y. Shen, D.M. Lanigan, J.M. Martin, X. Zhang, R.L. Axelbaum, *J. Mater. Chem. A* 4 (2016) 3538–3545.
- [87] K. Du, F. Yang, G.-R. Hu, Z.-D. Peng, Y.-B. Cao, K.S. Ryu, *J. Power Sources* 244 (2013) 29–34.
- [88] R. Yu, X. Wang, Y. Fu, L. Wang, S. Cai, M. Liu, B. Lu, G. Wang, D. Wang, Q. Ren, X. Yang, *J. Mater. Chem. A* 4 (2016) 4941–4951.
- [89] T.-F. Yi, Y.-M. Li, S.-Y. Yang, Y.-R. Zhu, Y. Xie, *ACS Appl. Mater. Interfaces* 8 (2016) 32349–32359.
- [90] H. Xu, S. Deng, G. Chen, *J. Mater. Chem. A* 2 (2014) 15015–15021.
- [91] X. Feng, Y. Gao, L. Ben, Z. Yang, Z. Wang, L. Chen, *J. Power Sources* 317 (2016) 74–80.
- [92] J. Billaud, D. Sheptyakov, S. Sallard, D. Leanza, M. Talianker, J. Grinblat, H. Sclar, D. Aurbach, P. Novak, C. Villevieille, *J. Mater. Chem. A* 7 (2019) 15215–15224.
- [93] H. Shang, F. Ning, B. Li, Y. Zuo, S. Lu, D. Xia, *ACS Appl. Mater. Interfaces* 10 (2018) 21349–21355.
- [94] M. Otoyama, Q. Jacquet, A. Iadecola, M. Saubanere, G. Rousse, J.-M. Tarascon, *Adv. Energy Mater.* 9 (2019) 1803674.
- [95] D. Liu, X. Fan, Z. Li, T. Liu, M. Sun, C. Qian, M. Ling, Y. Liu, C. Liang, *Nano Energy* 58 (2019) 786–796.
- [96] T.A. Wynn, C. Fang, M. Zhang, H. Liu, D.M. Davies, X. Wang, D. Lau, J.Z. Lee, B.-Y. Huang, K.-Z. Fung, C.-T. Ni, Y.S. Meng, *J. Mater. Chem. A* 6 (2018) 24651–24659.
- [97] G. Chen, J. An, Y. Meng, C. Yuan, B. Matthews, F. Dou, L. Shi, Y. Zhou, P. Song, G. Wu, D. Zhang, *Nano Energy* 57 (2019) 157–165.
- [98] Y. Liu, D. Ning, L. Zheng, Q. Zhang, L. Gu, R. Gao, J. Zhang, A. Franz, G. Schumacher, X. Liu, *J. Power Sources* 375 (2018) 1–10.
- [99] Q. Li, D. Zhou, L. Zhang, D. Ning, Z. Chen, Z. Xu, R. Gao, X. Liu, D. Xie, G. Schumacher, X. Liu, *Adv. Funct. Mater.* 29 (2019) 1806706.
- [100] Y. Liu, Z. Yang, J. Zhong, J. Li, R. Li, Y. Yu, F. Kang, *ACS Nano* 13 (2019) 11891–11901.
- [101] S. Hu, Y. Li, Y. Chen, J. Peng, T. Zhou, W.K. Pang, C. Didier, V.K. Peterson, H. Wang, Q. Li, Z. Guo, *Adv. Energy Mater.* 9 (2019) 1901795.
- [102] M. Xu, Z. Chen, L. Li, H. Zhu, Q. Zhao, L. Xu, N. Peng, L. Gong, *J. Power Sources* 281 (2015) 444–454.
- [103] C. Chen, T. Geng, C. Du, P. Zuo, X. Cheng, Y. Ma, G. Yin, *J. Power Sources* 331 (2016) 91–99.
- [104] B. Xiao, B. Wang, J. Liu, K. Kaliyappan, Q. Sun, Y. Liu, G. Dadheech, M.P. Balogh, L. Yang, T.-K. Sham, R. Li, M. Cai, X. Sun, *Nano Energy* 34 (2017) 120–130.
- [105] F. Wu, X. Zhang, T. Zhao, L. Li, M. Xie, R. Chen, *ACS Appl. Mater. Interfaces* 7 (2015) 3773–3781.
- [106] J. Ma, B. Li, L. An, H. Wei, X. Wang, P. Yu, D. Xia, *J. Power Sources* 277 (2015) 393–402.
- [107] Y. Lee, J. Lee, K.Y. Lee, J. Mun, J.K. Lee, W. Choi, *J. Power Sources* 315 (2016) 284–293.
- [108] D. Chen, F. Zheng, L. Li, M. Chen, X. Zhong, W. Li, L. Lu, *J. Power Sources* 341 (2017) 147–155.
- [109] J. Zhang, Q. Lu, J. Fang, J. Wang, J. Yang, Y. NuLi, *ACS Appl. Mater. Interfaces* 6 (2014) 17965–17973.
- [110] S. Zhao, B. Sun, K. Yan, J. Zhang, C. Wang, G. Wang, *ACS Appl. Mater. Interfaces* 10 (2018) 33260–33268.
- [111] J. Zheng, M. Gu, J. Xiao, B.J. Polzin, P. Yan, X. Chen, C. Wang, J.-G. Zhang, *Chem. Mater.* 26 (2014) 6320–6327.
- [112] H. Liu, C. Du, G. Yin, B. Song, P. Zuo, X. Cheng, Y. Maa, Y. Gao, *J. Mater. Chem. A* 2 (2014) 15640–15646.
- [113] B. Song, W. Li, P. Yan, S.-M. Oh, C.-M. Wang, A. Manthiram, *J. Power Sources* 325 (2016) 620–629.
- [114] M. Zhang, Z. Li, L. Yu, D. Kong, Y. Li, B. Cao, W. Zhao, J. Wen, F. Pan, *Nano Energy* 77 (2020) 105188.
- [115] M. Xu, Z. Chen, H. Zhu, X. Yan, L. Li, Q. Zhao, *J. Mater. Chem. A* 3 (2015) 13933–13945.
- [116] Y. Ma, P. Liu, Q. Xie, G. Zhang, H. Zheng, Y. Cai, Z. Li, L. Wang, Z.-Z. Zhu, L. Mai, D.-L. Peng, *Nano Energy* 59 (2019) 184–196.
- [117] W. Zhang, Y. Sun, H. Deng, J. Ma, Y. Zeng, Z. Zhu, Z. Lv, H. Xia, X. Ge, S. Cao, Y. Xiao, S. Xi, Y. Du, A. Cao, X. Chen, *Adv. Mater.* 32 (2020) 2000496.
- [118] B. Song, M.O. Lai, Z. Liu, H. Liu, L. Lu, *J. Mater. Chem. A* 1 (2013) 9954–9965.
- [119] L. Guo, J. Li, T. Cao, H. Wang, N. Zhao, F. He, C. Shi, C. He, E. Liu, *ACS Appl. Mater. Interfaces* 8 (2016) 24594–24602.
- [120] S.J. Han, B. Qiu, Z. Wei, Y.G. Xia, Z.P. Liu, *J. Power Sources* 268 (2014) 683–691.
- [121] M. Si, D. Wang, R. Zhao, D. Pan, C. Zhang, C. Yu, X. Lu, H. Zhao, Y. Bai, *Adv. Sci.* 7 (2020) 1902538.
- [122] X. Li, K. Zhang, D. Mitlin, Z. Yang, M. Wang, Y. Tang, F. Jiang, Y. Du, J. Zheng, *Chem. Mater.* 30 (2018) 2566–2573.
- [123] A. Dianat, N. Seriani, M. Bobeth, G. Cuniberti, *J. Mater. Chem. A* 1 (2013) 9273–9280.
- [124] P.K. Nayak, J. Grinblat, M. Levi, E. Levi, S. Kim, J.W. Choi, D. Aurbach, *Adv. Energy Mater.* 6 (2016) 1502398.

- [125] X. Ding, Y.-X. Li, X.-D. He, J.-Y. Liao, Q. Hu, F. Chen, X.-Q. Zhang, Y. Zhao, C.-H. Chen, ACS Appl. Mater. Interfaces 11 (2019) 31477–31483.
- [126] H. Zheng, Z. Hu, P. Liu, W. Xu, Q. Xie, W. He, Q. Luo, L. Wang, D. Gu, B. Qu, Z.-Z. Zhu, D.-L. Peng, Energy Storage Mater. 25 (2020) 76–85.
- [127] N. Zhang, J. Stark, H. Li, A. Liu, Y. Li, I. Hamam, J.R. Dahn, J. Electrochem. Soc. 167 (2020) 080518.
- [128] C.M. Subramaniam, H. Celio, K. Shiva, H.C. Gao, J.B. Goodenough, H.K. Liu, S. X. Dou, Sustain. Energy Fuels 1 (2017) 1292–1298.
- [129] D. Luo, X. Ding, J. Fan, Z. Zhang, P. Liu, X. Yang, J. Guo, S. Sun, Z. Lin, Angew. Chem. Int. Ed. 59 (2020) 23061–23066.
- [130] J. Zheng, X. Wu, Y. Yang, Electrochim. Acta 105 (2013) 200–208.
- [131] U. Breddemann, E.M. Erickson, V. Davis, F. Schipper, M. Ellwanger, M. Daub, A. Hoffmann, C. Erk, B. Markovsky, D. Aurbach, I. Krossing, Chemelectrochem 6 (2019) 3337–3349.
- [132] H.Z. Zhang, Q.Q. Qiao, G.R. Li, X.P. Gao, J. Mater. Chem. A 2 (2014) 7454–7460.
- [133] P. Hou, G. Li, X. Gao, J. Mater. Chem. A 4 (2016) 7689–7699.
- [134] E.M. Erickson, H. Sclar, F. Schipper, J. Liu, R. Tian, C. Ghanty, L. Burstein, N. Leifer, J. Grinblat, M. Talianker, J.-Y. Shin, J.K. Lampert, B. Markovsky, A.I. Frenkel, D. Aurbach, Adv. Energy Mater. 7 (2017) 1700708.
- [135] H.Z. Zhang, Q.Q. Qiao, G.R. Li, S.H. Ye, X.P. Gao, J. Mater. Chem. 22 (2012) 13104–13109.
- [136] X. Zheng, X. Wang, X. Cai, L. Xing, M. Xu, Y. Liao, X. Li, W. Li, ACS Appl. Mater. Interfaces 8 (2016) 30116–30125.
- [137] S. Tan, Z. Zhang, Y. Li, Y. Li, J. Zheng, Z. Zhou, Y. Yang, J. Electrochem. Soc. 160 (2012) A285–A292.
- [138] H. Li, J. Li, N. Zaker, N. Zhang, G.A. Botton, J.R. Dahn, J. Electrochem. Soc. 166 (2019) A1956–A1963.
- [139] S. Nakamura, A. Maljuk, Y. Maruyama, M. Nagao, S. Watauchi, T. Hayashi, Y. Anzai, Y. Furukawa, C.D. Ling, G. Deng, M. Aydeev, B. Buechner, I. Tanaka, Cryst. Growth Des. 19 (2019) 415–420.